



NAVAL POSTGRADUATE SCHOOL

MONTEREY, CALIFORNIA

THESIS

USV PATH PLANNING USING POTENTIAL FIELD MODEL

by

Nicholas A. Manzini

September 2017

Thesis Advisor:
Second Reader:

Brian Bingham
Xiaoping Yun

Approved for public release. Distribution is unlimited.

THIS PAGE INTENTIONALLY LEFT BLANK

REPORT DOCUMENTATION PAGE			<i>Form Approved OMB No. 0704-0188</i>	
Public reporting burden for this collection of information is estimated to average 1 hour per response, including the time for reviewing instruction, searching existing data sources, gathering and maintaining the data needed, and completing and reviewing the collection of information. Send comments regarding this burden estimate or any other aspect of this collection of information, including suggestions for reducing this burden, to Washington headquarters Services, Directorate for Information Operations and Reports, 1215 Jefferson Davis Highway, Suite 1204, Arlington, VA 22202-4302, and to the Office of Management and Budget, Paperwork Reduction Project (0704-0188) Washington, DC 20503.				
1. AGENCY USE ONLY (Leave blank)		2. REPORT DATE September 2017	3. REPORT TYPE AND DATES COVERED Master's thesis	
4. TITLE AND SUBTITLE USV PATH PLANNING USING POTENTIAL FIELD MODEL			5. FUNDING NUMBERS	
6. AUTHOR(S) Nicholas A. Manzini				
7. PERFORMING ORGANIZATION NAME(S) AND ADDRESS(ES) Naval Postgraduate School Monterey, CA 93943-5000			8. PERFORMING ORGANIZATION REPORT NUMBER	
9. SPONSORING /MONITORING AGENCY NAME(S) AND ADDRESS(ES) N/A			10. SPONSORING / MONITORING AGENCY REPORT NUMBER	
11. SUPPLEMENTARY NOTES The views expressed in this thesis are those of the author and do not reflect the official policy or position of the Department of Defense or the U.S. Government. IRB number N/A.				
12a. DISTRIBUTION / AVAILABILITY STATEMENT Approved for public release. Distribution is unlimited.			12b. DISTRIBUTION CODE	
13. ABSTRACT (maximum 200 words) This project aims to design, implement, and assess the performance of an unmanned surface vessel (USV) path planning with potential fields. The proposed algorithms are adaptations of the general potential field navigation method, tailored for the specific dynamics of USV path planning. A piecewise linear potential field model was implemented on a Clearpath USV using MATLAB and Simulink. The USV model and piecewise linear potential field model were tested in a Gazebo simulation and in the field. The simulations and real-world tests were compared to evaluate the performance of the potential field algorithms. The USV interacted with the repulsive and attractive fields successfully to maneuver around obstacles and boundaries to reach the objective.				
14. SUBJECT TERMS path planning, unmanned surface vehicles, potential field model			15. NUMBER OF PAGES 113	
			16. PRICE CODE	
17. SECURITY CLASSIFICATION OF REPORT Unclassified	18. SECURITY CLASSIFICATION OF THIS PAGE Unclassified	19. SECURITY CLASSIFICATION OF ABSTRACT Unclassified	20. LIMITATION OF ABSTRACT UU	

THIS PAGE INTENTIONALLY LEFT BLANK

Approved for public release. Distribution is unlimited.

USV PATH PLANNING USING POTENTIAL FIELD MODEL

Nicholas A. Manzini
Lieutenant Commander, United States Navy
B.S., Virginia Polytechnic Institute and State University, 2006

Submitted in partial fulfillment of the
requirements for the degree of

MASTER OF SCIENCE IN MECHANICAL ENGINEERING

from the

**NAVAL POSTGRADUATE SCHOOL
September 2017**

Approved by: Dr. Brian Bingham
Thesis Advisor

Dr. Xiaoping Yun
Second Reader

Dr. Garth V. Hobson
Chair, Department of Mechanical and Aerospace
Engineering

THIS PAGE INTENTIONALLY LEFT BLANK

ABSTRACT

This project aims to design, implement, and assess the performance of an unmanned surface vessel (USV) path planning with potential fields. The proposed algorithms are adaptations of the general potential field navigation method, tailored for the specific dynamics of USV path planning. A piecewise linear potential field model was implemented on a Clearpath USV using MATLAB and Simulink. The USV model and piecewise linear potential field model were tested in a Gazebo simulation and in the field. The simulations and real-world tests were compared to evaluate the performance of the potential field algorithms. The USV interacted with the repulsive and attractive fields successfully to maneuver around obstacles and boundaries to reach the objective.

THIS PAGE INTENTIONALLY LEFT BLANK

TABLE OF CONTENTS

I.	INTRODUCTION.....	1
A.	MOTIVATION.....	1
B.	PROBLEM STATEMENT.....	1
C.	PREVIOUS AND POTENTIAL APPLICATIONS OF UNMANNED SURFACE VEHICLES FOR THE NAVY.....	2
II.	BACKGROUND.....	5
A.	ARTIFICIAL POTENTIAL FIELD.....	5
1.	Parabolic Attractive Potential.....	6
2.	Parabolic Repulsive Potential.....	7
3.	Weaknesses of the Potential Field Method	8
B.	IMPLEMENTED POTENTIAL FIELD MODEL.....	9
1.	Reasons for Piecewise Linear Potential Field Model	15
2.	Modifications to Piecewise Linear Potential Field Model	15
III.	USV MODELING	21
A.	INTRODUCTION.....	21
B.	DYNAMIC MODEL OF THE USV	21
1.	Background.....	21
2.	Equations of Motion	21
C.	SYSTEM IDENTIFICATION.....	24
1.	Mass and Inertia.....	25
2.	Thrust Model	32
3.	Drag Coefficient Identification.....	35
4.	Model Parameters.....	43
D.	GAZEBO SIMULATION IMPLEMENTATION.....	44
IV.	EXPERIMENTAL RESULTS	45
A.	EXPERIMENTAL SETUP	45
1.	Load Cell Setup.....	45
2.	MATLAB and Simulink Setup	46
B.	GAZEBO EXPERIMENTAL RESULTS	52
C.	LAKE EL ESTERO EXPERIMENTAL RESULTS.....	58
D.	COMPARISON OF GAZEBO AND LAKE EL ESTERO RESULTS.....	76

V.	CONCLUSION	79
A.	SUMMARY OF RESULTS	79
B.	PROPOSAL FOR FUTURE STUDIES.....	79
	APPENDIX. THRUST COMMAND DATA	81
	LIST OF REFERENCES.....	91
	INITIAL DISTRIBUTION LIST	93

LIST OF FIGURES

Figure 1.	Clearpath Robotics USV.....	2
Figure 2.	U.S. Navy Minesweeping Drone from the Late 1960s. Source: [1].	3
Figure 3.	Model of Artificial Potential Field. Source: [5].	5
Figure 4.	Attractive Potential Field. Source: [4].....	7
Figure 5.	Repulsive Potential Field. Source: [4].....	8
Figure 6.	Attractive Potential Field. Adapted from [6].	10
Figure 7.	Repulsive Potential Field. Adapted from [6].....	12
Figure 8.	Combined Potential Field. Adapted from [6].	13
Figure 9.	Path of USV in Combined Potential Field. Adapted from [6].....	14
Figure 10.	Added Mass Surge Data for $V_{ss}=0.27$ m/s.....	27
Figure 11.	Added Mass Surge Data for $V_{ss}=0.81$ m/s.....	28
Figure 12.	Added Mass Surge Data for $V_{ss}=1.02$ m/s.....	29
Figure 13.	Added Inertia Yaw Data for $V_{ss}=0.16$ rad/s	30
Figure 14.	Added Inertia Yaw Data for $V_{ss}=0.25$ rad/s	31
Figure 15.	Forward Thrust Command 0.1	33
Figure 16.	Aft Thrust Command 0.2	34
Figure 17.	Thrust Command Relationship	35
Figure 18.	Steady State Surge Test	36
Figure 19.	Steady State Yaw Test.....	37
Figure 20.	Thruster Force versus Steady-State Velocity with Curves of Best Fit	38
Figure 21.	Torque versus Steady-State Angular Velocity with Curves of Best Fit	41

Figure 22.	USV Gazebo Simulation Environment.....	44
Figure 23.	Load Cell Calibration	45
Figure 24.	Control System Block Diagram.....	46
Figure 25.	Gazebo Simulation of Lake El Estero	47
Figure 26.	Lake El Estero. Adapted from [10].....	48
Figure 27.	USV Position and Attractive Force in Simulink Model	49
Figure 28.	Obstacle and Repulsive Force in Simulink Model	50
Figure 29.	Sum of Forces and Yaw/Speed Commands in Simulink Model.....	50
Figure 30.	Obstacle Radius of Influence Size.....	51
Figure 31.	USV Position with One Obstacle in Gazebo.....	52
Figure 32.	USV Command Yaw and Speed with One Obstacle in Gazebo	53
Figure 33.	USV Yaw and Speed with One Obstacle in Gazebo	54
Figure 34.	USV Position with Repulsive Channel and One Obstacle in Gazebo.....	55
Figure 35.	USV Command Yaw and Speed with Repulsive Channel and One Obstacle in Gazebo	56
Figure 36.	USV Yaw and Speed with Repulsive Channel and One Obstacle in Gazebo	57
Figure 37.	USV Position with One Obstacle	58
Figure 38.	USV Command Yaw and Speed with One Obstacle	59
Figure 39.	USV Yaw and Speed with One Obstacle.....	60
Figure 40.	USV Position with Three Obstacles.....	61
Figure 41.	USV Command Yaw and Speed with Three Obstacles.....	62
Figure 42.	USV Yaw and Speed with Three Obstacles	63
Figure 43.	.USV Return Trip with Three Obstacles.....	64
Figure 44.	USV Command Yaw and Speed with Three Obstacles.....	65

Figure 45.	USV Yaw and Speed with Three Obstacles	66
Figure 46.	USV Position with Repulsive Channel and One Obstacle	67
Figure 47.	USV Command Yaw and Speed with Repulsive Channel and One Obstacle	68
Figure 48.	USV Yaw and Speed with Repulsive Channel and One Obstacle	69
Figure 49.	USV Position with Repulsive Channel and One Obstacle	70
Figure 50.	USV Command Yaw and Speed with Repulsive Channel and One Obstacle	71
Figure 51.	USV Yaw and Speed with Repulsive Channel and One Obstacle	72
Figure 52.	USV Return Trip with Repulsive Channel and One Obstacle	73
Figure 53.	USV Command Yaw and Speed with Repulsive Channel and One Obstacle	74
Figure 54.	USV Yaw and Speed with Repulsive Channel and One Obstacle	75
Figure 55.	Combined USV Plots with One Obstacle.....	76
Figure 56.	Combined USV Plots with Repulsive Channel and One Obstacle	77
Figure 57.	Forward Thrust Command 0.2.....	81
Figure 58.	Forward Thrust Command 0.3.....	81
Figure 59.	Forward Thrust Command 0.4.....	82
Figure 60.	Forward Thrust Command 0.5.....	82
Figure 61.	Forward Thrust Command 0.6.....	83
Figure 62.	Forward Thrust Command 0.7.....	83
Figure 63.	Forward Thrust Command 0.8.....	84
Figure 64.	Forward Thrust Command 0.9.....	84
Figure 65.	Forward Thrust Command 1.0.....	85

Figure 66.	Aft Thrust Command 0.3	85
Figure 67.	Aft Thrust Command 0.4	86
Figure 68.	Aft Thrust Command 0.5	86
Figure 69.	Aft Thrust Command 0.6	87
Figure 70.	Aft Thrust Command 0.7	87
Figure 71.	Aft Thrust Command 0.8	88
Figure 72.	Aft Thrust Command 0.9	88
Figure 73.	Aft Thrust Command 1.0	89

LIST OF TABLES

Table 1.	USV Model Parameters.....	24
Table 2.	Curve Fit Results for Surge Added Mass Model.....	29
Table 3.	Curve Fit Results for Yaw Added Inertia Model.....	31
Table 4.	Curve Fit Results for Surge Drag Model with Goodness of Fit Metrics.....	39
Table 5.	Curve Fit Results for Yaw Drag Model with Goodness of Fit Metrics.....	42
Table 6.	Identified USV Model Values.....	43

THIS PAGE INTENTIONALLY LEFT BLANK

LIST OF ACRONYMS AND ABBREVIATIONS

BDA	battle damage assessment
DOF	degree of freedom
GPS	Global Positioning System
IMU	inertial measurement unit
ISR	intelligence, surveillance, and reconnaissance
USV	unmanned surface vehicle

THIS PAGE INTENTIONALLY LEFT BLANK

ACKNOWLEDGMENTS

I would like to thank my wife for her love, encouragement, and patience during my time at Naval Postgraduate School. I would also like to thank my family members who encouraged me to challenge myself and never stop learning. Finally, I would like to thank Dr. Brian Bingham for the invaluable experience of learning about and operating unmanned vehicles. I am forever grateful for your advice, guidance, and patience during the past year. It has truly been an honor and a pleasure.

THIS PAGE INTENTIONALLY LEFT BLANK

I. INTRODUCTION

A. MOTIVATION

There are many potential applications for robotic vehicles in defense and security. The Navy works with a variety of autonomous vehicles in restricted environments with limited intelligence about the areas. These platforms are force multipliers that can reduce the risk to personnel, conduct tasks that humans cannot, and be cost effective [1]. The ability for the vehicles to maneuver safely and efficiently in a coordinated manner while collecting data is invaluable. Path planning is a fundamental capability for simultaneous operation and obstacle avoidance of such systems. One specific method for path planning is to use potential field algorithms to avoid obstacles, prevent collisions, travel to waypoints, and surround objects of interest. This thesis will involve the development of potential field based path planning for an unmanned surface vehicle (USV) to transit safely around obstacles and reach a specified location.

B. PROBLEM STATEMENT

The objective of this research is to design, implement, and assess the performance of USV path planning using potential fields. Piecewise linear potential fields were applied in computer simulations and field experiments using the Clearpath Robotics USV pictured in Figure 1 [2]. The attractive potential fields (targets) and repulsive potential fields (obstacles) were modeled as circles. The repulsive boundary lines were developed as perpendicular potential fields. Evaluating local minima was not in the scope of this research due to the focus of developing a dynamic model of the USV and testing it using potential field algorithms.



Figure 1. Clearpath Robotics USV

C. PREVIOUS AND POTENTIAL APPLICATIONS OF UNMANNED SURFACE VEHICLES FOR THE NAVY

The United States Navy has been developing and using USVs since the end of World War II to conduct minesweeping, as shown in Figure 2, and battle damage assessment (BDA) operations [1]. These vehicles were remotely controlled and lacked autonomous capabilities, but reduced the risk to manned forces while accomplishing the mission.

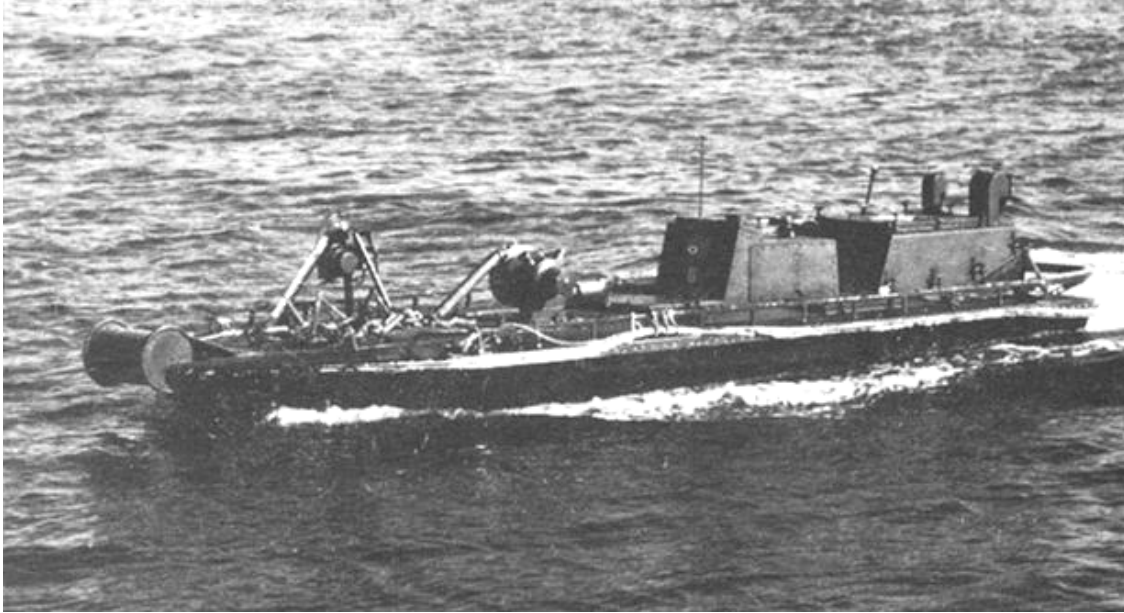


Figure 2. U.S. Navy Minesweeping Drone from the Late 1960s.
Source: [1].

The Navy has continued to develop and expand the use of unmanned systems through experimentation and experience. Minesweeping capabilities have increased through further automation, longer operational time, and larger coordinated search patterns. USVs are being used for intelligence, surveillance, and reconnaissance (ISR) missions in high-risk areas with different levels of autonomy [1].

In [1], the Navy has stated that all USVs must have the ability to autonomously avoid obstacles and that technical development is needed in this area. Potential field algorithms have been gaining in popularity for use in obstacle and collision avoidance and path planning. The algorithms could be implemented to enable the USVs to surround enemy vessels at a specific distance, escort or protect friendly vessels, and transit with other manned or unmanned platforms [3].

THIS PAGE INTENTIONALLY LEFT BLANK

II. BACKGROUND

A. ARTIFICIAL POTENTIAL FIELD

In [4], Latombe describes the potential function as the sum of the attractive potential and repulsive potential energies acting on the robot. The robot, which is treated as a point in the configuration space, is pulled by the attractive potential toward a defined target and pushed away from obstacles by the repulsive potential. The potential field forces are shown in Figure 3.

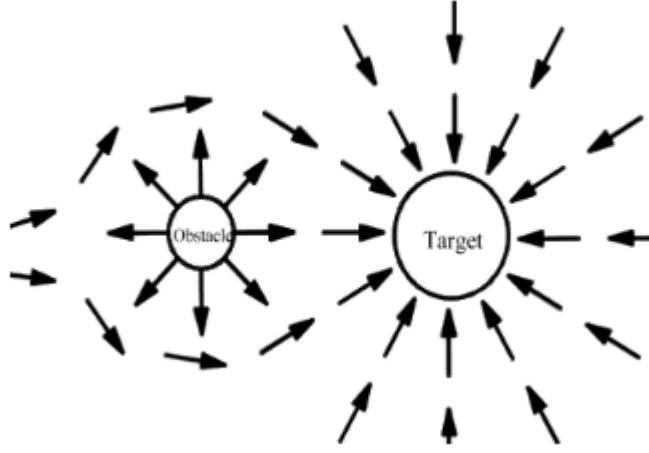


Figure 3. Model of Artificial Potential Field. Source: [5].

The motion planning of the potential function is performed iteratively by calculating the artificial force $\vec{F}(q) = -\vec{\nabla}U(q)$ induced by the potential function at each iteration, where \vec{F} is the force vector and $\vec{\nabla}U$ is the gradient of the potential field function. A path is generated along the direction of motion of the artificial force at each increment [4].

The basic potential functions are summed in order to make the robot attracted toward targets and repulsed by obstacles:

$$U(q) = U_{att}(q) + U_{rep}(q), \quad (1)$$

where U_{att} is the attractive potential and U_{rep} is the repulsive potential [4]. The gradient function of the attractive and repulsive forces are

$$\vec{F}_{att} = -\vec{\nabla}U_{att} , \quad (2)$$

$$\vec{F}_{rep} = -\vec{\nabla}U_{rep} , \quad (3)$$

$$\vec{F} = \vec{F}_{att} + \vec{F}_{rep} , \quad (4)$$

where \vec{F} is the sum of the two vectors [4]. Specifying the appropriate potential functions, which generate the virtual forces on a robotic platform, is critical to the application of the method.

1. Parabolic Attractive Potential

One common attractive potential function is a parabolic function [4]. In such an implementation the potential function is

$$U_{att}(q) = \frac{1}{2} \varepsilon \rho_{goal}^2(q) , \quad (5)$$

where ε is a positive gain factor of attraction and ρ_{goal} is the distance between the robot and the goal $\|q - q_{goal}\|$. When the robot reaches the goal $U_{att}(q_{goal}) = 0$ [4]. The derivation of the attractive force from the potential is:

$$\begin{aligned} \vec{F}_{att}(q) &= -\vec{\nabla}U_{att}(q) \\ &= -\varepsilon \rho_{goal}(q) \vec{\nabla} \rho_{goal}(q) \\ &= -\varepsilon (q - q_{goal}) , \end{aligned} \quad (6)$$

where \vec{F}_{att} converges linearly as the robot gets closer to the goal [4]. Figure 4 shows an attractive potential field.

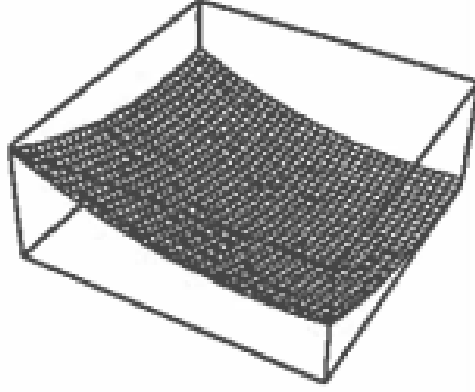


Figure 4. Attractive Potential Field. Source: [4].

2. Parabolic Repulsive Potential

Similarly, a common repulsive potential function is:

$$U_{rep}(q) = \begin{cases} \frac{1}{2} \eta \left(\frac{1}{\rho(q)} - \frac{1}{\rho_0} \right)^2 & \text{if } \rho(q) \leq \rho_0 \\ 0 & \text{if } \rho(q) > \rho_0 \end{cases} \quad (7)$$

where η is a positive gain factor of repulsion and $\rho(q)$ is the distance between the robot and the obstacle $\|q - q_{obstacle}\|$ [4]. The repulsive potential field of an obstacle is designed to not influence the robot when it is outside the distance of influence ρ_0 .

The derivation of the repulsive force from the potential is:

$$\begin{aligned}\vec{F}_{rep}(q) &= -\vec{\nabla}U_{rep}(q) \\ &= \begin{cases} \eta\left(\frac{1}{\rho(q)} - \frac{1}{\rho_0}\right) \frac{1}{\rho^2(q)} \vec{\nabla}\rho(q) & \text{if } \rho(q) \leq \rho_0 \\ 0 & \text{if } \rho(q) > \rho_0 \end{cases} \quad (8)\end{aligned}$$

Once the robot is inside the distance of influence, the repulsive force is positive and goes to infinity as the robot moves closer to the obstacle [4]. Figure 5 displays a repulsive potential field.

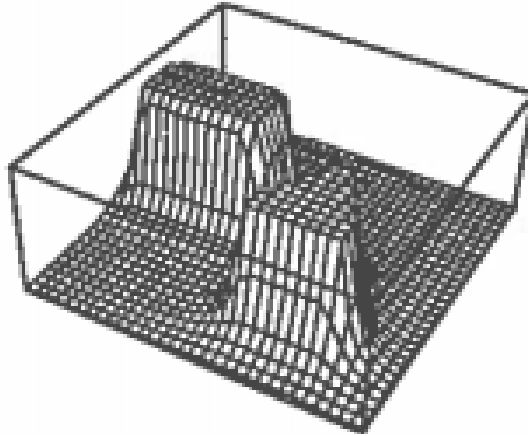


Figure 5. Repulsive Potential Field. Source: [4].

3. Weaknesses of the Potential Field Method

The weaknesses of the artificial potential field method are that at certain points during the transit of the robot \vec{F} may be zero [5]. This could cause the robot to stop moving or circle around a point and is called the local minimum of the potential function [5]. In addition, the potential field path of the robot may not converge when there are too many obstacles. The robot would then not be able to reach the goal or target [5].

The issue of local minima can be reduced by designing a function that limits how many local minima are present or provides a method to escape from the local minimum [4].

B. IMPLEMENTED POTENTIAL FIELD MODEL

The potential field that was selected for the Clearpath Robotics USV was based upon Goodrich's piecewise linear potential field algorithm in [6]. It was selected due to the flexibility and simplicity of implementing the piecewise linear potential fields in MATLAB and Simulink. The piecewise linear equations could be modified for different geometries, and the strength of the fields was easily adjusted. The attractive force is calculated by finding the distance between the goal and the USV:

$$d = \sqrt{(x_G - x)^2 + (y - y_G)^2} , \quad (9)$$

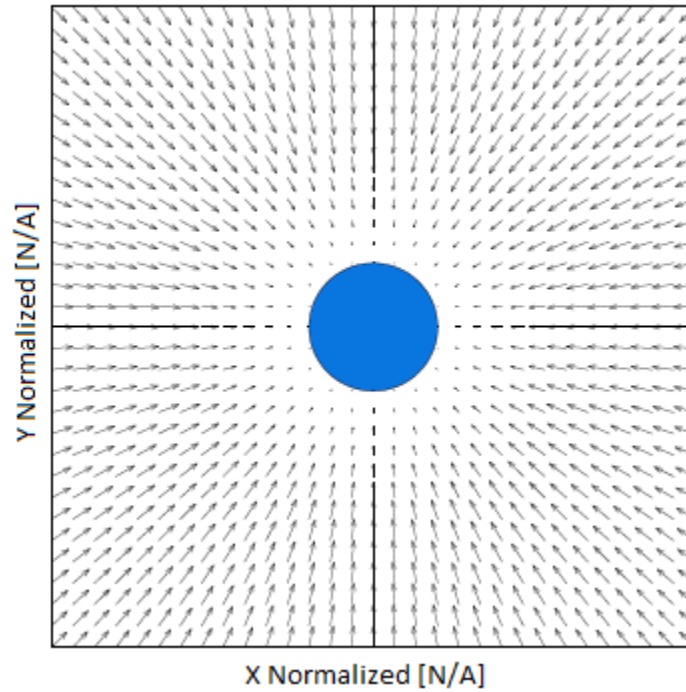
where x_G and y_G is the position of the goal and x and y is the position of the USV. The angle between the USV and the goal is determined by

$$\theta = \tan^{-1}\left(\frac{y_G - y}{x_G - x}\right) . \quad (10)$$

The forces in the x and y directions are evaluated using an if-else if statement:

$$\begin{aligned} \text{if } d < r & \quad \Delta x = \Delta y = 0 \\ \text{if } r \leq d \leq s + r & \quad \Delta x = \alpha(d - r) \cos(\theta) \quad \text{and} \quad \Delta y = \alpha(d - r) \sin(\theta) \\ \text{if } d > s + r & \quad \Delta x = \alpha s \cos(\theta) \quad \text{and} \quad \Delta y = \alpha s \sin(\theta). \end{aligned} \quad (11)$$

The goal is modeled as a blue circle with radius r in Figure 6, and when the USV is inside the radius, there are no forces acting upon it. The attractive field has a radius of influence s and the USV senses a proportion of the max force when it is between r and $s+r$. Outside the radius of influence, the max attractive force acts on the USV and drives it toward the goal. This is shown in Figure 6. The arrows represent the magnitude and direction of the attractive potential field. A constant positive gain α is included to scale the strength of the attractive force [6].



The blue circle is an attractive potential field or a goal of the USV.

Figure 6. Attractive Potential Field. Adapted from [6].

The repulsive force is calculated by finding the distance between the obstacle and the USV:

$$d = \sqrt{(x_o - x)^2 + (y - y_o)^2} , \quad (12)$$

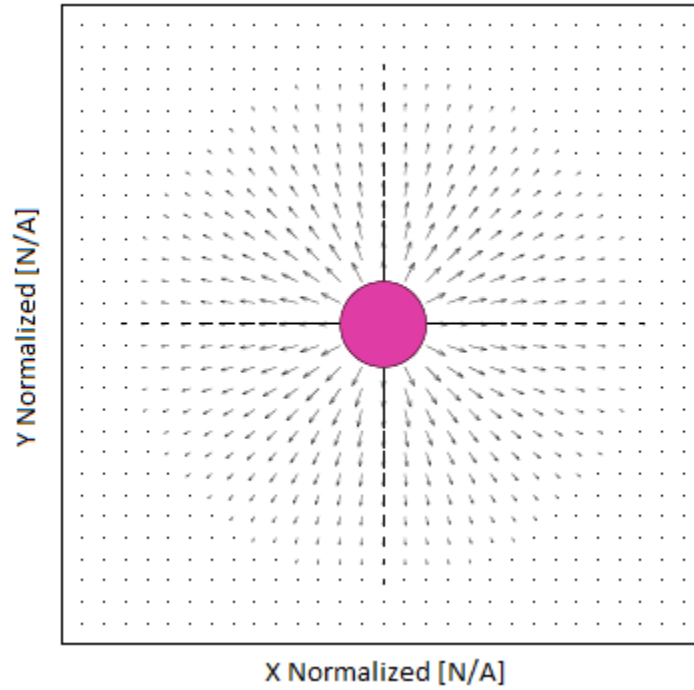
where x_o and y_o is the position of the obstacle and x and y is the position of the USV. The angle between the USV and the obstacle is determined by

$$\theta = \tan^{-1}\left(\frac{y_o - y}{x_o - x}\right). \quad (13)$$

The forces in the x and y directions (Δx and Δy respectfully) are evaluated using an if-else if statement:

$$\begin{aligned} \text{if } d < r & \quad \Delta x = -(\cos(\theta))\infty \quad \text{and} \quad \Delta y = -(\sin(\theta))\infty \\ \text{if } r \leq d \leq s + r & \quad \Delta x = -\beta(s + r - d)\cos(\theta) \quad \text{and} \quad \Delta y = -\beta(s + r - d)\sin(\theta) \\ \text{if } d > s + r & \quad \Delta x = \Delta y = 0. \end{aligned} \quad (14)$$

The obstacle is modeled as a pink circle in Figure 7 with radius r and when the USV is inside the radius the max repulsive force acts on it. The repulsive field has a radius of influence s and the USV senses a proportion of the max force when it is between r and $s+r$. Outside the radius of influence, the repulsive potential field is zero in order to prevent an obstacle from interfering with the USV path and is presented in Figure 7. The arrows represent the magnitude and direction of the repulsive potential field. A constant positive gain β is included to scale the strength of the repulsive force [6].



The pink circle is a repulsive potential field or an obstacle for the USV.

Figure 7. Repulsive Potential Field. Adapted from [6].

The repulsive and attractive vectors are combined to find:

$$\begin{aligned}\Delta x &= \Delta_o x + \Delta_G x \\ \Delta y &= \Delta_o y + \Delta_G y.\end{aligned}\tag{15}$$

The formulations in Equations (11), (14), and (15) are used to generate the combined potential field with an obstacle and goal displayed in Figure 8. The brown circle is a repulsive potential field or an obstacle for the USV. The green circle is an attractive potential field or a goal for the USV. The arrows represent the magnitude and direction of the combined potential fields.

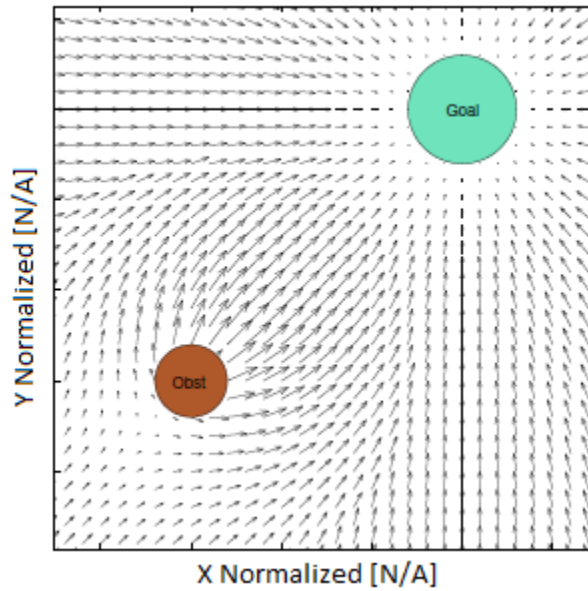


Figure 8. Combined Potential Field. Adapted from [6].

A possible path for the USV to transit around the obstacle (green circle) and reach the goal (pink circle) is represented in Figure 9. The arrows represent the magnitude and direction of the combined potential fields. The black line is a possible path for the USV to travel.

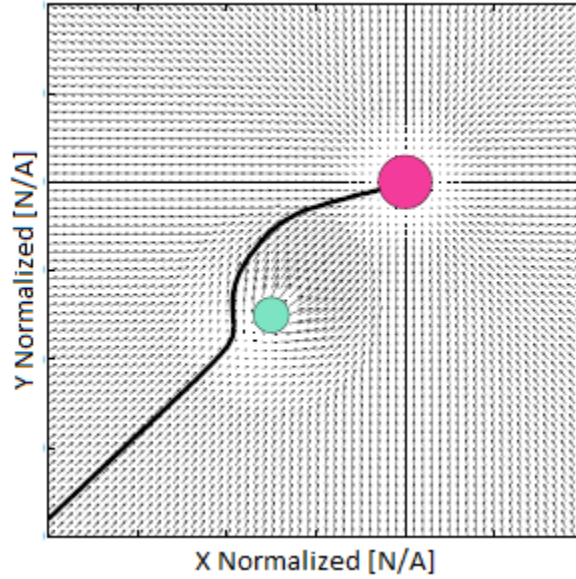


Figure 9. Path of USV in Combined Potential Field. Adapted from [6].

The combined potential field vectors, Δx and Δy , generated in Equation (15) are used to find:

$$v = \sqrt{\Delta x^2 + \Delta y^2} , \quad (16)$$

$$\theta = \tan^{-1} \left(\frac{\Delta y}{\Delta x} \right) , \quad (17)$$

where v is the velocity of the USV and θ is the direction of the USV. The USV maneuvers around the environment interacting with the potential fields and selecting new directions and speeds to reach the goal [6].

1. Reasons for Piecewise Linear Potential Field Model

The piecewise linear potential field model was selected due to the ease of incorporating the repulsive and attractive forces. The size and radius of influence of the obstacles and goals was very explicit and able to be adjusted appropriately. MATLAB and Simulink were chosen to implement the high-level potential field control and the piecewise linear formulas were straightforward and intuitive.

2. Modifications to Piecewise Linear Potential Field Model

Goodrich's formulas were adapted to run in MATLAB and Simulink by calculating the magnitude of the attractive and repulsive forces and then determining the vector components. This was done to provide traceability from the angle between the USV and the goal (θ) and the vector components back to the magnitudes of the potential forces in Simulink. Troubleshooting methods were simplified by being able to determine if there were errors in the forces or the angles of the goals and obstacles. The attractive force had the following changes:

$$d = \sqrt{(x_G - x)^2 + (y_G - y)^2} , \quad (18)$$

$$\begin{aligned} \text{if } d < r & \quad F_{\text{attractive}} = 0 \\ \text{if } r \leq d \leq s + r & \quad F_{\text{attractive}} = F_{\text{max}} \frac{(d-r)}{s} \\ \text{if } d > s + r & \quad F_{\text{attractive}} = F_{\text{max}} \end{aligned} \quad (19)$$

where F_{max} is the constant positive gain of the attractive force. The angle between the USV and the goal was calculated as in Equation (10).

The magnitude of the attractive force was determined first and then separated into the following vector components

$$\begin{aligned}\Delta_G x &= F_{attractive_x} = F_{attractive} \cos(\theta), \\ \Delta_G y &= F_{attractive_y} = F_{attractive} \sin(\theta).\end{aligned}\tag{20}$$

The repulsive force had similar changes and is expressed as:

$$d = \sqrt{(x_o - x)^2 + (y_o - y)^2}, \tag{21}$$

$$\begin{aligned}\text{if } d < r & \quad F_{repulsive} = -F_{\max} \\ \text{if } r \leq d \leq s + r & \quad F_{repulsive} = -F_{\max} \left(1 - \frac{(d-r)}{s}\right) \\ \text{if } d > s + r & \quad F_{repulsive} = 0\end{aligned}\tag{22}$$

where F_{\max} is the constant positive gain of the repulsive force. The angle between the USV and the obstacle was calculated as in Equation (13).

This potential field implementation provides the high-level path planning for the USV, but to do so, the output of the path planning must interface with the low-level USV feedback control. For the Clearpath USV, the interface to the low-level control takes the form of a “course command,” which includes a forward (surge) velocity and a yaw. For the purposes of implementation, the force vector must be converted from the potential field path planning (force in the x and y direction) into a course command (surge velocity and yaw).

The magnitude of the repulsive force was determined first and then separated into the vector components:

$$\begin{aligned}\Delta_O x &= F_{repulsive_x} = F_{repulsive} \cos(\theta), \\ \Delta_O y &= F_{repulsive_y} = F_{repulsive} \sin(\theta).\end{aligned}\tag{23}$$

The vector forces were then summed to find the total potential force in the x and y directions:

$$\begin{aligned}\Delta x &= \Delta_O x + \Delta_G x = F_x = F_{repulsive_x} + F_{attractive_x}, \\ \Delta y &= \Delta_O y + \Delta_G y = F_y = F_{repulsive_y} + F_{attractive_y}.\end{aligned}\tag{24}$$

The yaw of the USV was calculated in radians, using the force components:

$$\theta = \tan^{-1}\left(\frac{F_y}{F_x}\right).\tag{25}$$

The speed of the USV is proportional to the magnitude of the potential force:

$$Speed_{USV} = \sqrt{F_x^2 + F_y^2}.\tag{26}$$

The yaw and speed adjust as the attractive and repulsive forces act on the position of the USV.

Repulsive potential line obstacles were also developed to provide boundaries to the USV. The end points of each boundary were selected and the slope of the line was calculated by:

$$\begin{aligned}
 & \text{if } |x_{end} - x_{start}| < 0.01 \\
 & \quad slope = 1 \times 10^6 \\
 & \text{else} \\
 & \quad slope = \frac{y_{end} - y_{start}}{x_{end} - x_{start}}
 \end{aligned} \tag{27}$$

where x_{end} / y_{end} and x_{start} / y_{start} are the points of the boundaries. The slope was evaluated using an if-else statement to ensure that if the boundary was a vertical line, the slope would be given a set value of 1×10^6 . This was to prevent any error being carried forward in the MATLAB calculations.

The slope of the boundary line was used to determine the perpendicular intersection of the current USV position and the boundary line. An if-else if statement was developed to calculate the intersection points:

$$\begin{aligned}
 & \text{if } slope = 0 \\
 & \quad y_{int} = y_{start} \\
 & \quad x_{int} = x_{USV} \\
 & \text{elseif } |slope| > 1000 \\
 & \quad y_{int} = y_{USV} \\
 & \quad x_{int} = x_{start} \\
 & \text{else} \\
 & \quad x_{int} = \left(\frac{slope}{slope^2 + 1} \right) (y_{usv} - y_{start} + slope * x_{start} + \frac{x_{usv}}{slope}) \\
 & \quad y_{int} = (y_{start} + slope * (x_{int} - x_{start}))
 \end{aligned} \tag{28}$$

where $x_{\text{int}} / y_{\text{int}}$ are the intersection points and $x_{\text{USV}} / y_{\text{USV}}$ is the position of the USV.

The USV position and the intersection points were calculated to evaluate the distance, d , from the USV to the boundary line:

$$d = \sqrt{(x_{\text{USV}} - x_{\text{int}})^2 + (y_{\text{USV}} - y_{\text{int}})^2} . \quad (29)$$

The repulsive potential field boundary line is modeled as having two parallel areas of influence, that each has a different repulsive force acting on the USV if it is inside the area. Outside the areas, the repulsive potential field is zero.

An if-else if statement is used to determine the magnitude of the force acting on the USV:

$$\begin{aligned} &\text{if } d < \text{boundary1} \\ &\quad F_{\text{repulsive}} = F_{\text{max}} \\ &\text{elseif } d \leq (\text{boundary1} + \text{boundary2}) \\ &\quad F_{\text{repulsive}} = F_{\text{max}} \left(1 - \frac{(d - \text{boundary1})}{\text{boundary2}}\right) \\ &\text{else} \\ &\quad F_{\text{repulsive}} = 0 \end{aligned} \quad (30)$$

where boundary1 and boundary2 are the parallel areas of influence.

The angle between the USV and the boundary line, θ , is determined by

$$\theta = \tan^{-1} \left(\frac{y_{\text{USV}} - y_{\text{int}}}{x_{\text{USV}} - x_{\text{int}}} \right) . \quad (31)$$

The magnitude of the repulsive line force was determined first and then separated into the vector line components:

$$\begin{aligned}\Delta_{line}x &= F_{repulsive_x} = F_{repulsive} \cos(\theta), \\ \Delta_{line}y &= F_{repulsive_y} = F_{repulsive} \sin(\theta),\end{aligned}\tag{32}$$

where $\Delta_{line}x$ and $\Delta_{line}y$ are the repulsive line vector forces. The vector forces from the lines, goal, and obstacle were then summed to find the total potential force in the x and y directions:

$$\begin{aligned}\Delta x &= \Delta_Ox + \Delta_Gx + \Delta_{line}x = F_x = F_{repulsive_x} + F_{attractive_x}, \\ \Delta y &= \Delta_Oy + \Delta_Gy + \Delta_{line}y = F_y = F_{repulsive_y} + F_{attractive_y}.\end{aligned}\tag{33}$$

The yaw of the USV was calculated in radians using the force components:

$$\theta = \tan^{-1}\left(\frac{F_y}{F_x}\right).\tag{34}$$

The speed of the USV is proportional to the magnitude of the potential force:

$$Speed_{USV} = \sqrt{F_x^2 + F_y^2}.\tag{35}$$

The yaw and speed adjust as the attractive and repulsive forces act on the position of the USV.

III. USV MODELING

A. INTRODUCTION

To support development and early testing of the path-planning algorithms described in Chapter II, a simulation was required to represent the USV dynamics in a virtual environment. Without a simulation, field testing is the only method for design iteration, and such field tests are time consuming, resource intensive and limited in the types of scenarios to be tested. For the simulation to be useful it is necessary that the simulated dynamics be similar to that of the actual vessel, hence the need to model the physical parameters of the Clearpath USV.

B. DYNAMIC MODEL OF THE USV

1. Background

The maneuvering models described by Fossen [7], [8] are the basis for many USV models. The references contain a number of different generic models and extensions of these models for specific cases. The focus tends to be on full-sized surface ships and platforms, but the underlying equations are also relevant to small USVs.

2. Equations of Motion

This model contains second-order (linear and quadratic) terms for the dissipative terms. In this section, the notation and process followed is detailed in [7], Chapter VII. The 3 degrees of freedom (DOF), horizontal-plane maneuvering model uses the state vector $\nu = [u, v, r]^T$ where the velocities u, v , and r are in the surge, sway, and yaw directions, respectively. The velocities are considered to be relative to an irrotational constant ocean current.

The nonlinear maneuvering equations from [7] are

$$M_{RB}\dot{v} + C_{RB}(v)v + M_A\dot{v}_r + C_A(v_r)v_r + D(v_r)v_r = \tau + \tau_{wind} + \tau_{waves}, \quad (36)$$

where v_r is the velocity vector relative to an irrotational water current v_c , i.e., $v = v_r + v_c$. The linear and quadratic drag terms from [7] are

$$D(v_r) = \begin{bmatrix} X_u + X_{u|u}|u| & 0 & 0 \\ 0 & Y_v + Y_{v|v}|v| & Y_r + Y_{r|r}|r| \\ 0 & N_v + N_{v|v}|v| & N_r + N_{r|r}|r| \end{bmatrix}. \quad (37)$$

In [9], the Blanke model is used with the addition of the linear drag terms. The simplified speed equation in the surge direction is

$$\underbrace{(m - X_{\ddot{u}})\dot{u}}_{RB \text{ and } AM \text{ inertia}} = \underbrace{X_u u + X_{u|u}|u|u}_{Drag} + \underbrace{\tau(c)}_{Thrust}. \quad (38)$$

The steering equation in the sway direction is

$$\underbrace{(m - Y_{\ddot{v}})\dot{v}}_{RB \text{ and } AM \text{ inertia}} = - \underbrace{(m - Y_{ur})ur}_{RB \text{ and } AM \text{ Coriolis}} + \underbrace{Y_v v + Y_{v|v}|v|v}_{Drag}, \quad (39)$$

and in the yaw direction it is

$$\underbrace{(I_z - N_{\ddot{r}})\dot{r}}_{RB \text{ and } AM \text{ inertia}} = \underbrace{N_r r + N_{r|r}|r|r}_{Drag} + \underbrace{T(c)}_{Torque}, \quad (40)$$

where c is the associated thrust command in Equations (38) and (40).

The following assumptions are made:

- Speed: Surge
 - The Coriolis terms $(m + X_{vr})vr$, both rigid body and added mass contributions, are negligible because the sway speed is much less than the surge speed.
 - The centripetal terms $(mx_g + X_{rr})r^2$ are neglected on the assumption of a low turn rate.
- Steering: Sway and Yaw
 - The rigid body and added mass coupling terms are neglected.
 - $(mx_g - Y_{\dot{r}})\dot{r}$ in the sway equation
 - $(mx_g - N_{\dot{v}})\dot{v}$ in the yaw equation
 - The rigid body and added mass Coriolis terms are neglected.
 - $-(mx_g - N_{ur})ur$ in the yaw equation
 - The coupled drag terms are neglected because they are negligible.
 - $Y_{uv}uv$ and $Y_{|v|r}|v|r$ in the sway equation
 - $N_{uv}uv$ and $N_{|v|r}|v|r$ in the yaw equation
 - The quadratic term $N_{|v|v}|v|v$ in the Blanke model is substituted with a linear and quadratic term as a function of yaw, $N_r r + N_{|r|r}|r|r$.

C. SYSTEM IDENTIFICATION

Given the equations of motion in (38-40), the next step in developing a model of the Clearpath USV is to experimentally identify as many of the parameters of the model as possible. Table 1 describes the parameters and methods of identification.

Table 1. USV Model Parameters

Description	Variable	Identification Method
Rigid Body Mass	m	Scale
Added Mass, Surge	$X_{\ddot{u}}$	Dynamic Surge Test
Linear Drag, Surge	$X_u u$	Steady-State Surge Test
Quadratic Drag, Surge	$X_{ u u} u u$	Steady-State Surge Test
Thrust, Surge	$\tau(c)$	Bollard Pull Test
Added Mass, Sway	$Y_{\ddot{v}}$	Not Identified
Added Mass Coriolis, Sway	Y_{ur}	Not Identified
Linear Drag, Sway	$Y_v v$	Not Identified
Quadratic Drag, Sway	$Y_{ v v} v v$	Not Identified
Rigid Body Inertia, Yaw	I_z	Moment of Inertia Calculation
Added Mass Inertia, Yaw	$N_{\ddot{r}}$	Dynamic Yaw Test
Linear Drag, Yaw	$N_r r$	Steady-State Yaw Test
Quadratic Drag, Yaw	$N_{r r} r r$	Steady-State Yaw Test
Torque, Yaw	$T(c)$	Bollard Pull Test and Calculation

The sway parameters were not identified in Table 1 due to the sway speed being negligible when compared to the surge speed.

1. Mass and Inertia

a. Rigid Body Mass and Moment Inertia

The mass of the Clearpath USV is 36.0 kg as measured with a spring scale. The mass of the Clearpath USV according to the technical specifications is 28.0 kg with no payload [2]. The moment of inertia of the USV was assumed to be the form of a simple box with the plane about the center. The estimated moment of inertia is

$$I = \frac{m(b^2 + w^2)}{12} = \frac{36(1.35^2 + 0.98^2)}{12} = 8.35 \text{ kg} \cdot \text{m}^2. \quad (41)$$

b. Added Mass and Added Inertia

The general form of the surge and yaw models in Equations (38) and (40) is

$$m\dot{y} + k_1 y + k_2 y^2 = F, \quad (42)$$

where $y(t)$ is the forward speed or yaw rate, m is the inertia, k_1 is the linear drag term, k_2 is the quadratic term, and F is the constant thrust or torque. In Section 3 below, the linear term, k_1 , can be neglected for the Clearpath USV. For a constant input, F , the solution to the differential equation (42) takes the form of

$$y(t) = y_{ss} \tanh\left(y_{ss} \frac{k_2}{m} t\right), \quad (43)$$

where y_{ss} is the steady state velocity. The drag coefficient, k_1 , from the steady-state experiment results is known, so there are two unknown parameters, the total inertia (m) (which includes the sum of the rigid body and added mass) and the steady-state velocity (y_{ss}).

To estimate these two parameters, the inertia and the steady-state velocity, step-response tests were conducted on the USV. Starting at zero velocity, the USV was given constant thrust commands and allowed to reach steady state velocity. Once the USV was at a steady, consistent velocity, the input command was stopped and the USV decelerated on its own. This procedure was repeated at discrete levels of thrust and then the curve in Equation (42) was fit to the experimental data by finding values of y_{ss} and m to minimize the error between the model of Equation (42) and the data.

For the surge direction, at three discrete input levels, the results of this process are presented in Figure 10 through Figure 12. The added mass in the surge direction was calculated using Equation (38), and the mass data is tabulated in Table 2.

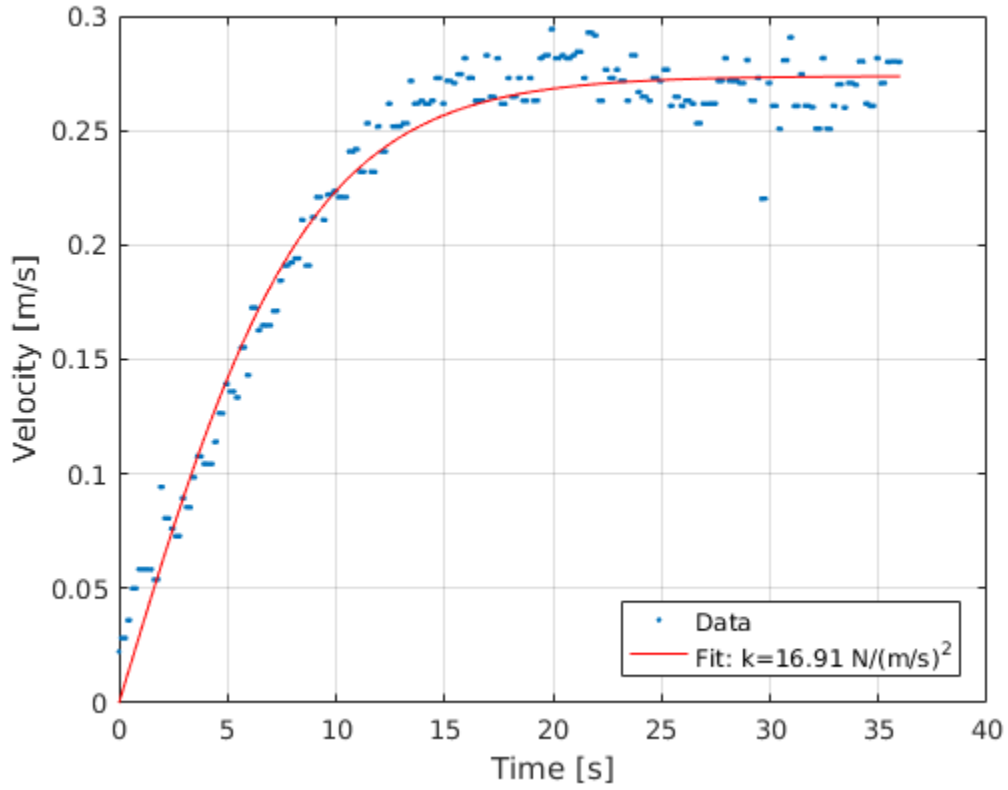


Figure 10. Added Mass Surge Data for $V_{ss}=0.27 \text{ m/s}$

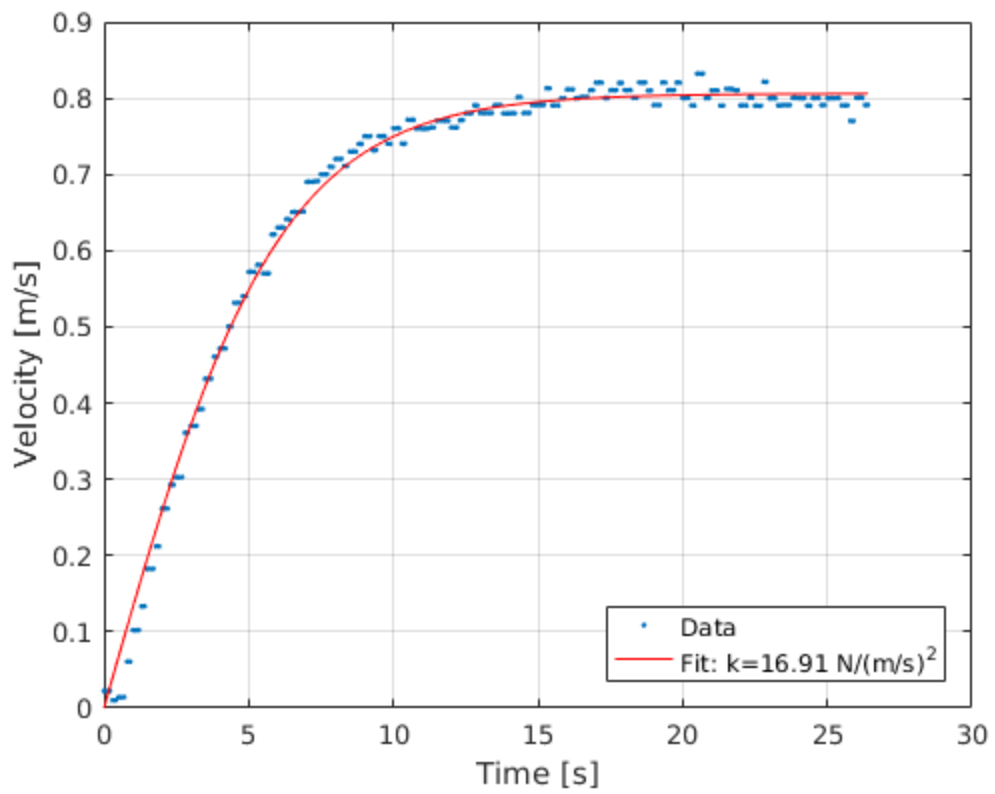


Figure 11. Added Mass Surge Data for $V_{ss}=0.81 \text{ m/s}$

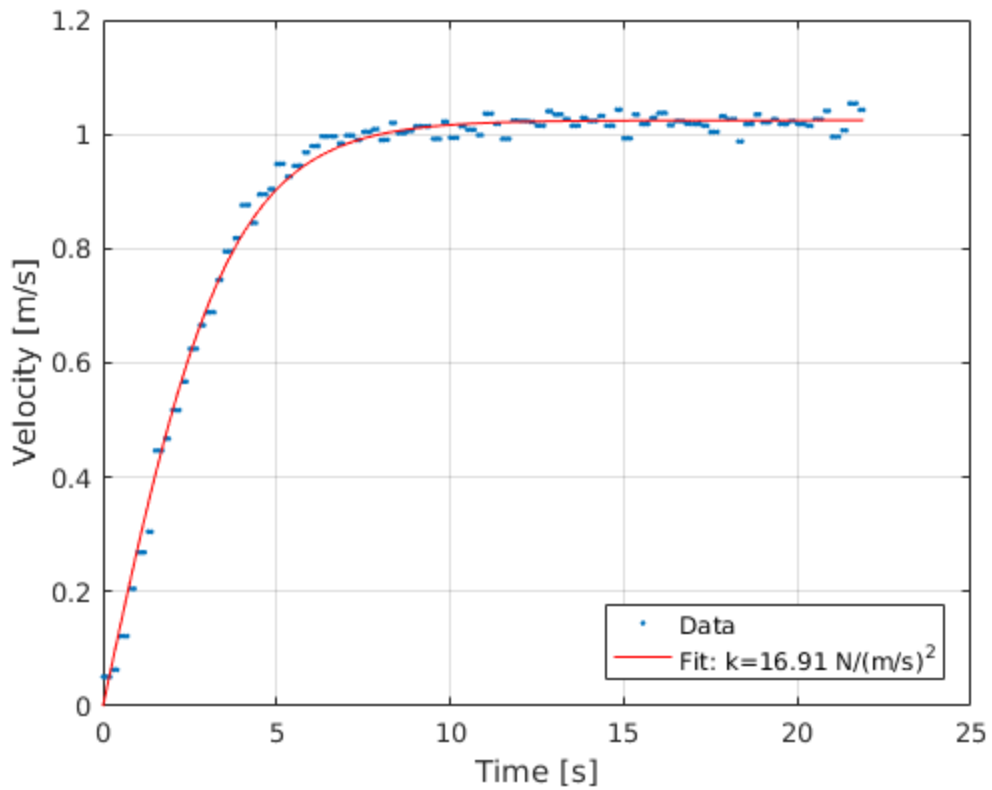


Figure 12. Added Mass Surge Data for $V_{ss}=1.02$ m/s

Table 2. Curve Fit Results for Surge Added Mass Model

Surge Fit Data			
Vss (m/s)	0.27	0.81	1.02
95% Confidence Bounds for Vss (m/s)	0.27, 0.28	0.80, 0.81	1.02, 1.03
Mass (kg)	40.40	82.20	62.57
95% Confidence Bounds for Mass (kg)	39.12, 41.67	80.85, 83.54	61.48, 63.66

The added mass for three different steady-state velocities is displayed in Table 2. The mass increased as the velocity increased until the steady-state velocity reached 1.02 m/s. The added mass decreased from 82.20 to 62.57 kg at 1.02 m/s. Confidence bounds were also calculated for the steady-state velocities and the added mass.

For the yaw direction, the USV was given torque commands to spin in a clockwise circle and allowed to reach steady state angular velocity. Once the USV was at a steady, consistent angular velocity, the input command was stopped, and the USV decelerated on its own. The step response in yaw was measured. The result is data for each step response experiment. MATLAB was used to fit a curve to the data, which is presented in Figure 13 and Figure 14. The added inertia in the yaw direction was determined using Equation (40), and the inertia data is tabulated in Table 3.

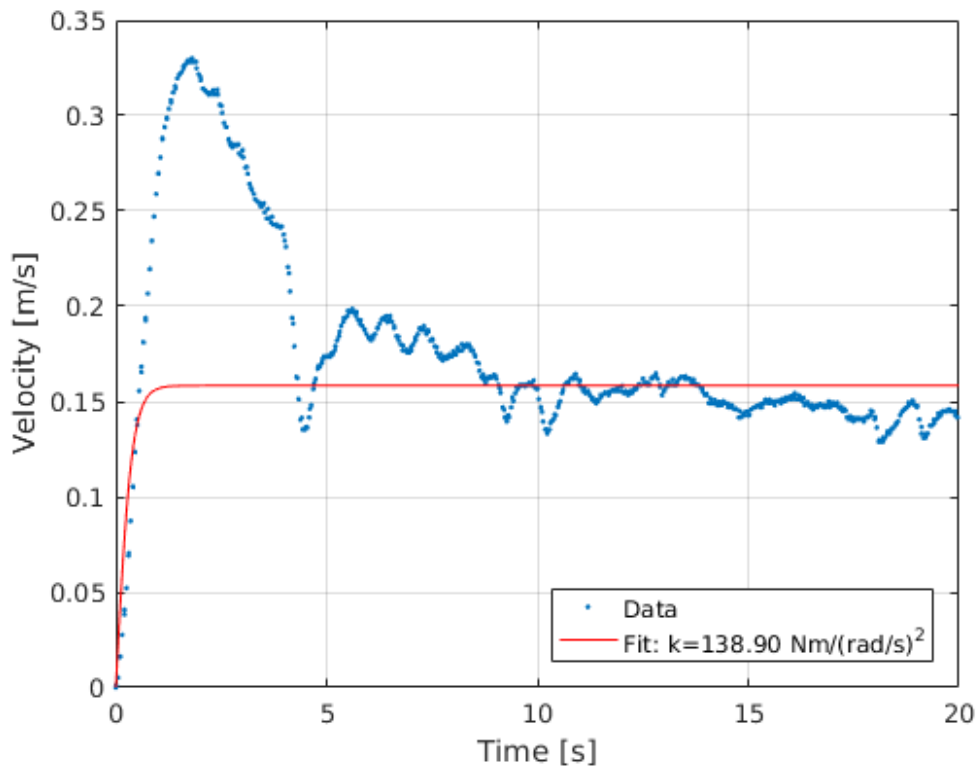


Figure 13. Added Inertia Yaw Data for $V_{ss}=0.16$ rad/s

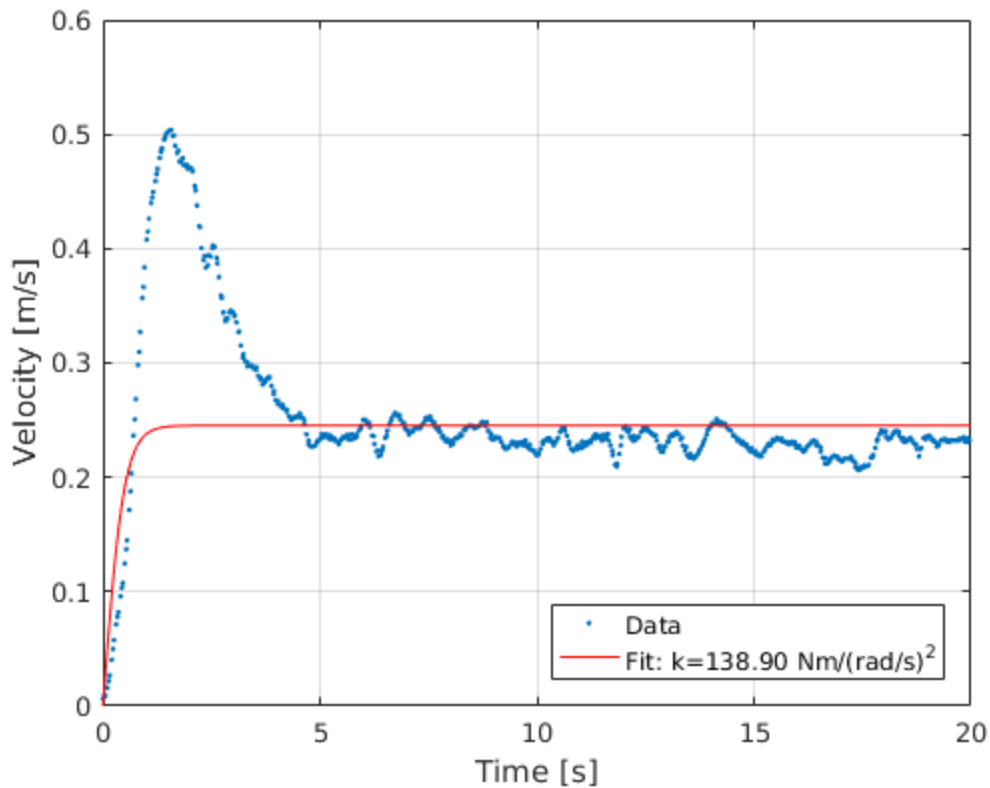


Figure 14. Added Inertia Yaw Data for $V_{ss}=0.25$ rad/s

Table 3. Curve Fit Results for Yaw Added Inertia Model

Yaw Fit Data		
Vss (rad/s)	0.16	0.25
95% Confidence Bounds for Vss (rad/s)	0.16, 0.16	0.24, 0.25
Moment of Inertia (kg*m²)	8.32	16.38
95% Confidence Bounds for Inertia (kg*m²)	5.73, 10.92	13.12, 19.64

The added moment of inertia for two different steady-state angular velocities is displayed in Table 3. The inertia nearly doubled from 8.32 to 16.38 kg*m², as the angular velocity increased from 0.16 to 0.25 rad/s. Confidence

bounds were also calculated for the steady-state angular velocities and the added inertia.

2. Thrust Model

The thrust generated by each of the two thrusters on the USV is a function of the motor command given to the onboard motor controller. Typically, this motor command is proportional to the voltage of the internal motor. In this section the functional relationship between the thrust command, a value between -1.0 (reverse) and 1.0 (forward), and the resulting thrust force generated by the thruster assembly on the Clearpath USV is identified.

A bollard pull test was performed in the CAVR test tank to evaluate this relationship. The USV was given thrust commands from -1.0 (reverse) to 1.0 (forward) while statically attached to the side of the CAVR test tank with a load cell in line with mooring. The voltage output from the load cell was recorded with a 16-bit analog-to-digital data acquisition system and the calibration in Figure 17 was used to estimate the force generated at discrete thrust commands.

The forward thrust command of 0.1 and calculated forces are presented in Figure 15. The mean force and standard deviation were calculated for each trial and are displayed in the legend. Figures for each of the forward command trials are located in the Appendix.

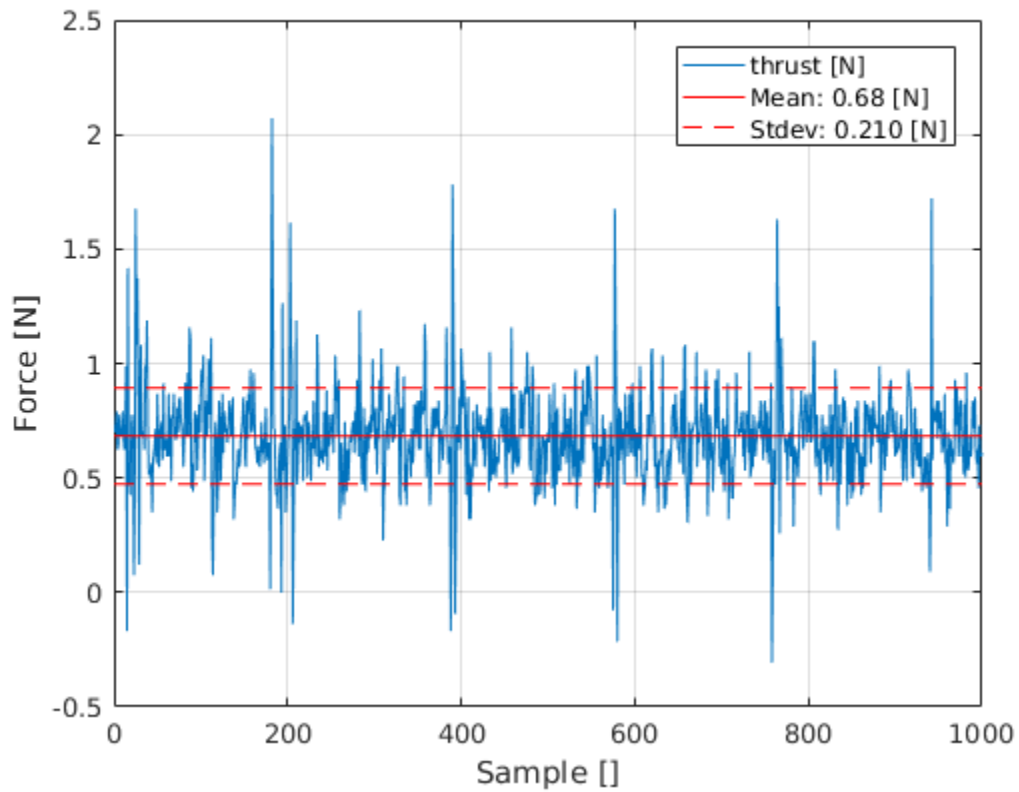


Figure 15. Forward Thrust Command 0.1

The same procedure was repeated for discrete values of reverse thrust. The example in Figure 16 shows the results for a reverse thrust of 0.2 and the graphs for the other values of the reverse thrust trials are included in the Appendix.

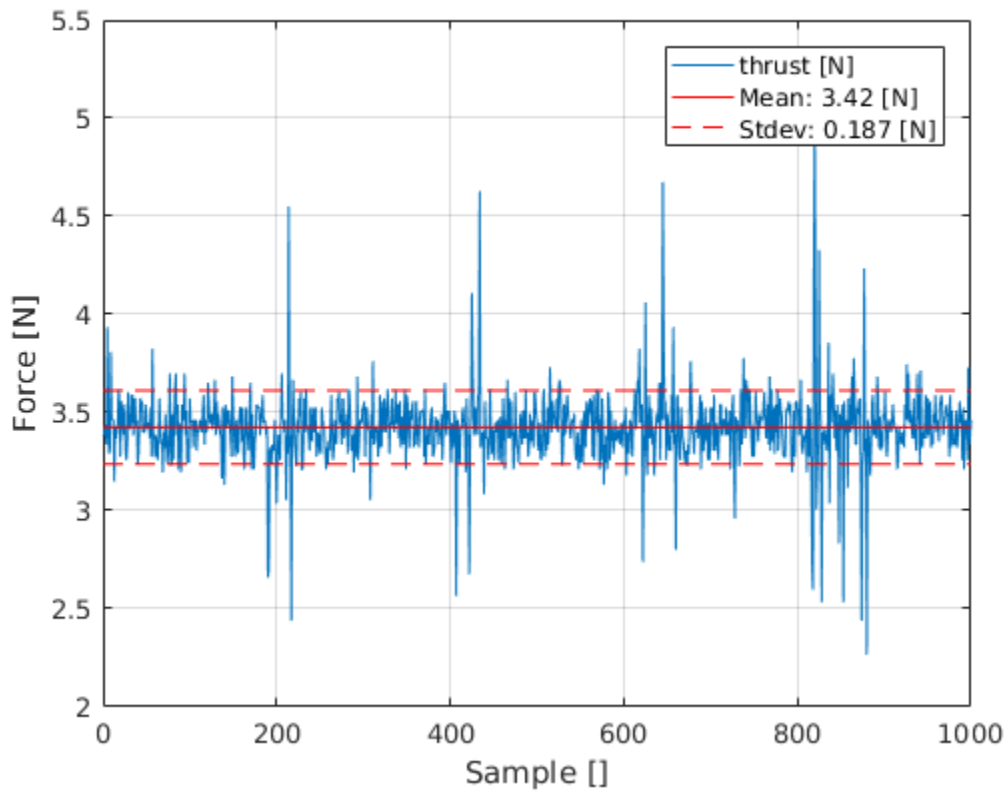


Figure 16. Aft Thrust Command 0.2

A time-series of the load cell force is generated for each level of commanded thrust with N values between -1.0 and 1.0. The mean thrust standard deviation is estimated from the time-series. Figure 17 illustrates these values for the range of thrust commands. A line of best fit was determined to show the relationship between the commands and the static forces. The line of best fit in Figure 17 shows a non-linear relationship between the commands and outputted thrust. The plot is not symmetric and illustrates the lack of reverse thrust of the USV. The forward thrust direction is much more effective and increases until settling out at 40.0 N.

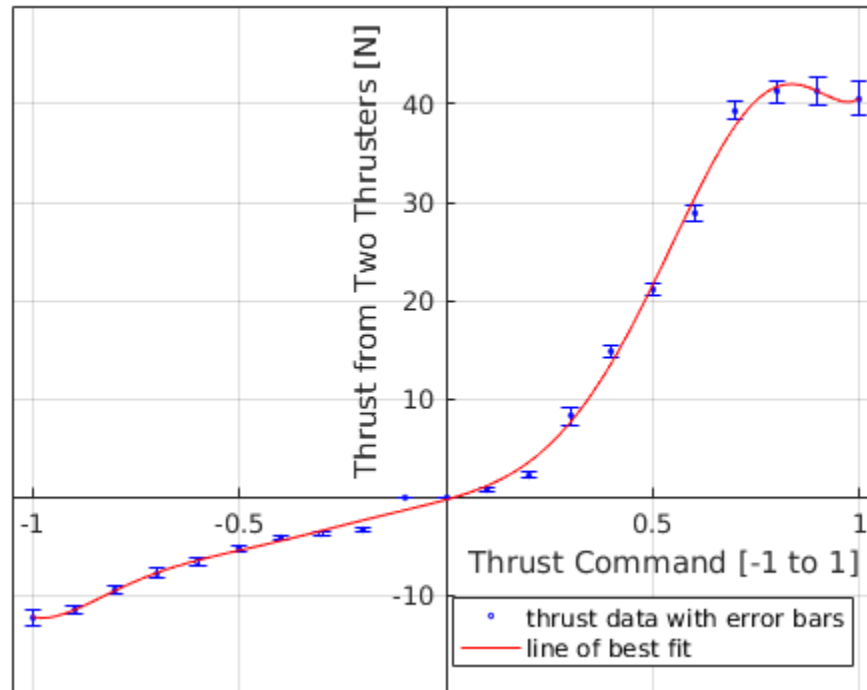


Figure 17. Thrust Command Relationship

3. Drag Coefficient Identification

To estimate the hydrodynamic drag terms in the USV model from Equations (38) and (40), a series of steady-state velocity tests were completed in the surge and yaw directions of motion. For each test, a constant input (thrust for surge and torque for yaw) was imposed and the steady-state velocity (forward

velocity and angular velocity) was measured by the onboard inertial measurement unit (IMU)/Global Positioning System (GPS) sensor. The relationship between constant input and steady-state velocity is then used to estimate the coefficients of drag.

The mean steady state surge and yaw values were interpolated for each thrust command. The data along with a curve of best fit is displayed in Figure 18 and Figure 19.

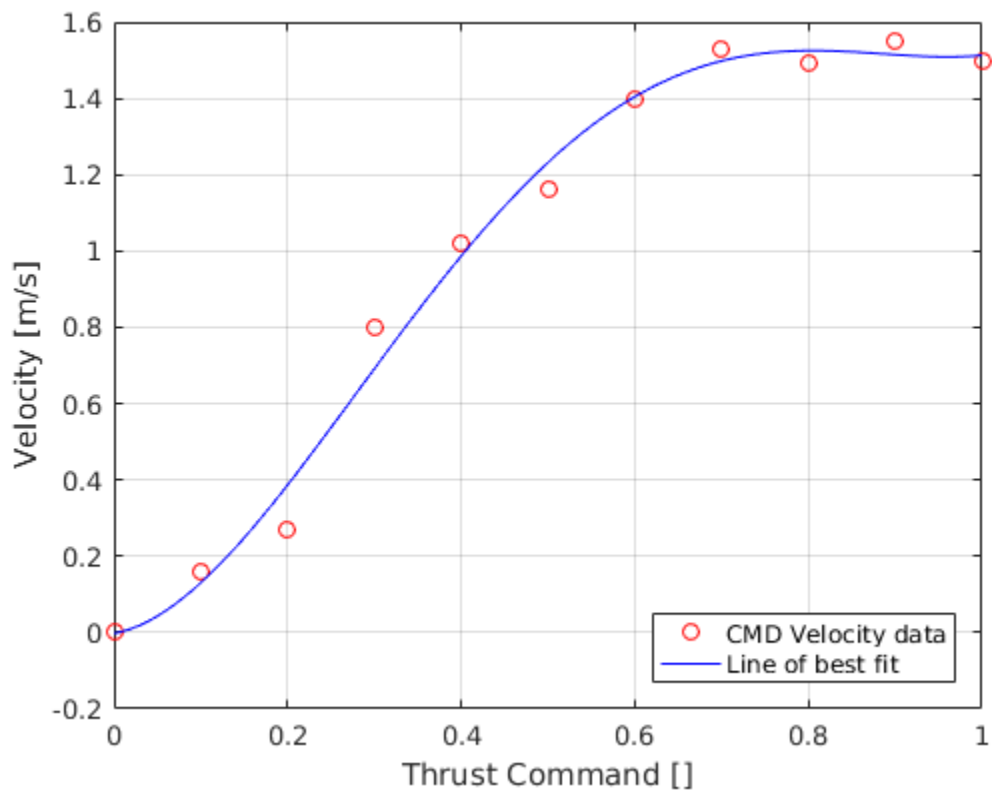


Figure 18. Steady State Surge Test

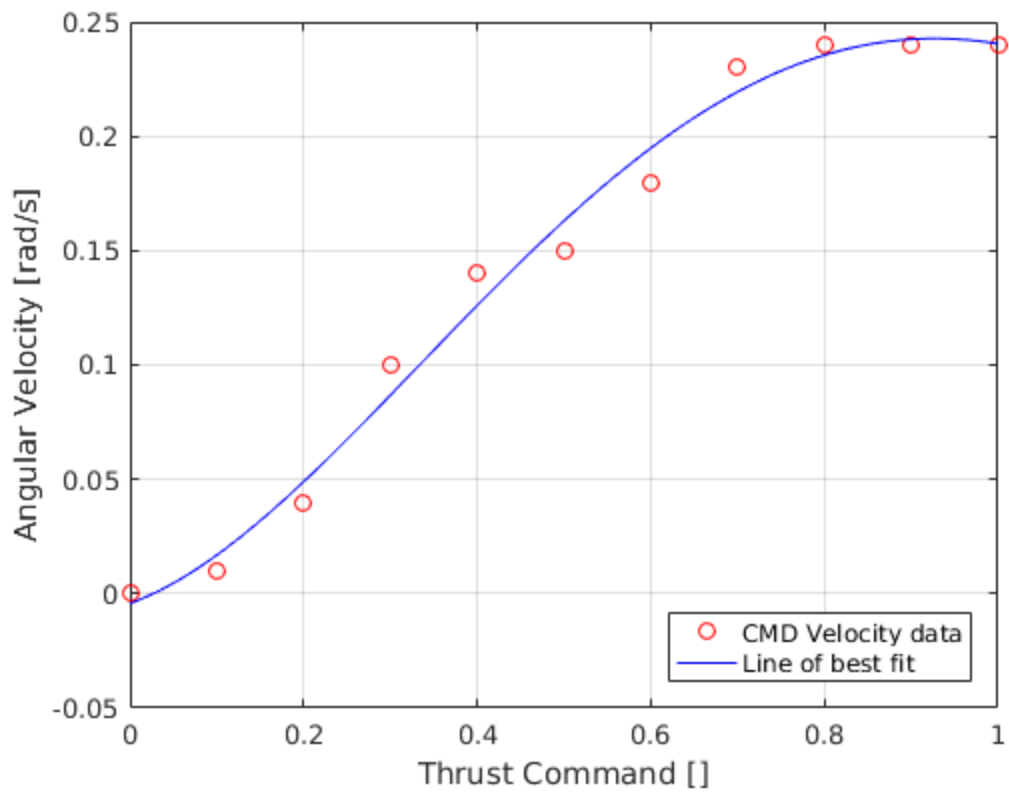


Figure 19. Steady State Yaw Test

The thrust command curve presented in Figure 17 was used to estimate the thrust/torque that correlated with the thrust commands for each test. This allows us to examine the relationship between velocity and thrust force and angular velocity and total torque. Figure 20 is the total thrust force versus steady state forward speed and Figure 21 is the total torque versus steady state yaw rate.

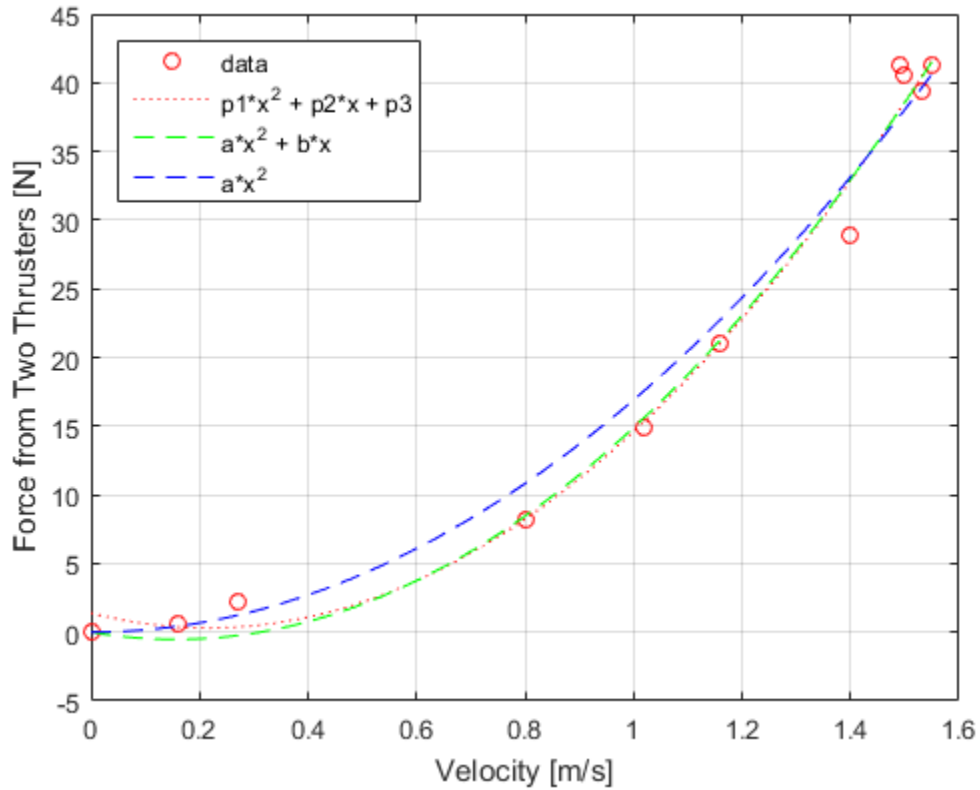


Figure 20. Thruster Force versus Steady-State Velocity with Curves of Best Fit

The curves of best fit for Figure 20 are

$$fo(x) = 23.24x^2 - 10.04x + 1.395, \quad (44)$$

$$fo(x) = 21.62x^2 - 6.736x, \quad (45)$$

$$fo(x) = 16.91x^2. \quad (46)$$

Table 4 quantifies three possible models for the hydrodynamic drag in the surge direction. The models each contain a subset of the following parameters:

- a: quadratic coefficient
- b: linear coefficient
- c: constant coefficient.

Table 4. Curve Fit Results for Surge Drag Model with Goodness of Fit Metrics

Drag Model Formulas for the Fit	Coefficients	95% Confidence Bounds	Sum of Squares due to Error (SSE)	Adjusted R ²	Root Mean Square Error (RMSE)
Polynomial: $fo(x)=a*x^2+b*x+c$	a=23.24	15.96, 30.52	37.1464	0.9846	2.1548
	b=-10.04	-22.17, 2.081			
	c=1.395	-2.359, 5.149			
Linear + Quadratic: $fo(x)=a*x^2+b*x$	a=21.62	15.98, 27.27	40.5551	0.9850	2.1228
	b=-6.736	-14.69, 1.22			
Quadratic Only $fo(x)=a*x^2$	a=16.91	15.91, 17.9	57.0866	0.9810	2.3893

As the number of coefficients in the drag model are reduced, the goodness-of-fit metrics indicate a reduction in the agreement between the drag model and the observed data. The model that includes all three terms (Polynomial) has a non-zero constant term (c) which would suggest that the USV would have a non-zero forward velocity with no applied force, which is not consistent with experimental evidence. The Linear+Quadratic model results include a linear coefficient (b) that is negative, which is also not physically consistent with the operation of the USV. Furthermore, the goodness-of-fit metrics suggest that the quality of the fit for the Quadratic Only model is similar to that of the Polynomial and Linear+Quadratic formulations. The Quadratic Only model of drag in the surge direction was used due to the consistency of the physical operation, small change in fit quality, and the qualitative assessment of Figure 20. Therefore, the model terms in Equation (38) are

$$X_u u = 0, \quad (47)$$

$$X_{|u|u} |u| u = 16.9 \text{ N} / (m / s)^2. \quad (48)$$

The curves of best fit for Figure 21 are

$$to(x) = 93.86x^2 + 10.35x - 0.077, \quad (49)$$

$$to(x) = 97.15x^2 + 9.265x, \quad (50)$$

$$to(x) = 138.9x^2. \quad (51)$$

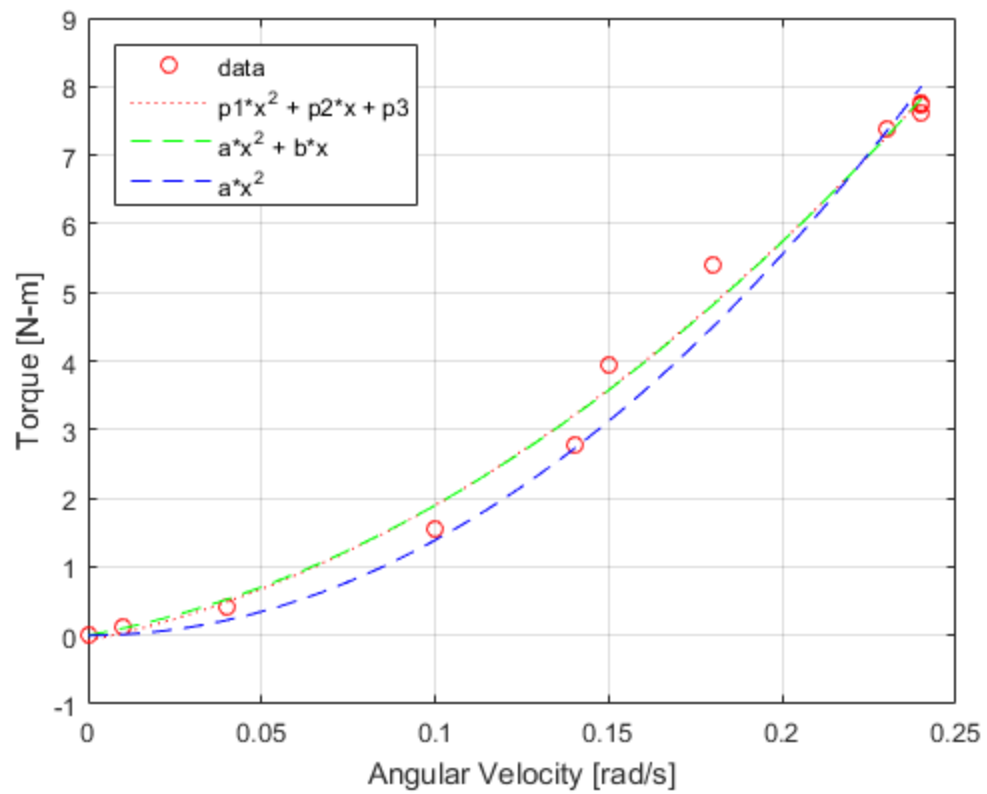


Figure 21. Torque versus Steady-State Angular Velocity with Curves of Best Fit

The results of model fitting for the yaw drag experiments are reported in Table 5.

Table 5. Curve Fit Results for Yaw Drag Model with Goodness of Fit Metrics

Drag Model Formulas for the Fit	Coefficients	95% Confidence Bounds	Sum of Squares due to Error (SSE)	Adjusted R ²	Root Mean Square Error (RMSE)
Polynomial: to(x)=a*x ² +b*x+c	a=93.86	54.39, 133.3	0.8666	0.9898	0.3291
	b=10.35	0.07937, 20.63			
	c=-0.07664	-0.6026, 0.4493			
Linear+ Quadratic to(x)=a*x ² +b*x	a=97.15	67, 127.3	0.8788	0.9908	0.3125
	b=9.265	2.699, 15.83			
Quadratic Only to(x)=a*x ²	a=138.9	131, 146.8	1.8738	0.9823	0.4329

The same reasoning as described for the surge drag model identification is followed. For the yaw case, it could be argued that the Linear+Quadratic model should be used because it more closely agrees with the experimental results, as shown in Figure 21. The Quadratic Only model has been chosen for consistency and since it simplifies the identification of the added mass and provides an acceptable goodness-of-fit. The resulting model parameters from Equation (40) are

$$N_r r = 0, \quad (52)$$

$$N_{r|r} |r| = 139 \text{ Nm} / (\text{rad} / \text{s})^2. \quad (53)$$

4. Model Parameters

The calculated model parameters identified in Sections 1 through 3 in this chapter are collected in Table 6.

Table 6. Identified USV Model Values

Description	Variable	Value [units]
Rigid Body Mass	m	36.0 kg
Added Mass, Surge	$X_{\ddot{u}}$	61.7 kg (mean from Table 2)
Linear Drag, Surge	$X_{u\dot{u}}$	0.0 $N / (m / s)$
Quadratic Drag, Surge	$X_{ u \dot{u}}$	16.9 $N / (m / s)^2$
Thrust, Surge	$\tau(c)$	Figure 20
Added Mass, Sway	$Y_{\ddot{v}}$	N/A
Added Mass Coriolis, Sway	Y_{ur}	N/A
Linear Drag, Sway	$Y_{v\dot{v}}$	N/A
Quadratic Drag, Sway	$Y_{ v \dot{v}}$	N/A
Rigid Body Inertia, Yaw	I_z	8.35 $kg \cdot m^2$
Added Mass Inertia, Yaw	$N_{\ddot{r}}$	12.4 $kg \cdot m^2$ (mean from Table 3)
Linear Drag, Yaw	$N_{r\dot{r}}$	0.0 $N \cdot m / (rad / s)$
Quadratic Drag, Yaw	$N_{ r \dot{r}}$	139.0 $N \cdot m / (rad / s)^2$
Torque, Yaw	$T(c)$	Figure 21

D. GAZEBO SIMULATION IMPLEMENTATION

The Clearpath USV is a 3 DOF model while the Gazebo simulation that was developed is a 6 DOF model. For simulation purposes, only the maneuvering model is necessary. The inertia and damping values are assumed for roll and pitch, respectively. In the heave direction, a constant cross section for the buoyancy calculation and a damping coefficient are assumed. The Gazebo USV plug-in is presented in Figure 22.

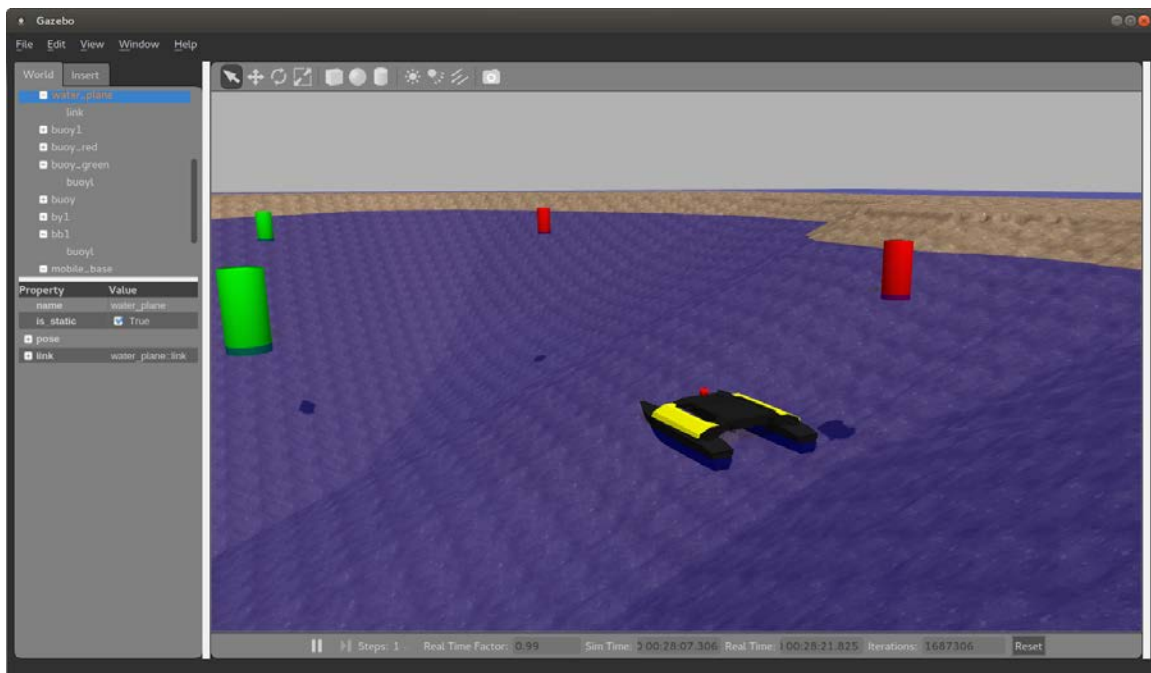


Figure 22. USV Gazebo Simulation Environment

IV. EXPERIMENTAL RESULTS

A. EXPERIMENTAL SETUP

1. Load Cell Setup

A load cell was calibrated using measured weights and connected to a multifunction data acquisition module. The external and load voltages were measured along with the force in units of newton. The calibration data along with the line of best fit equation is shown in Figure 23.

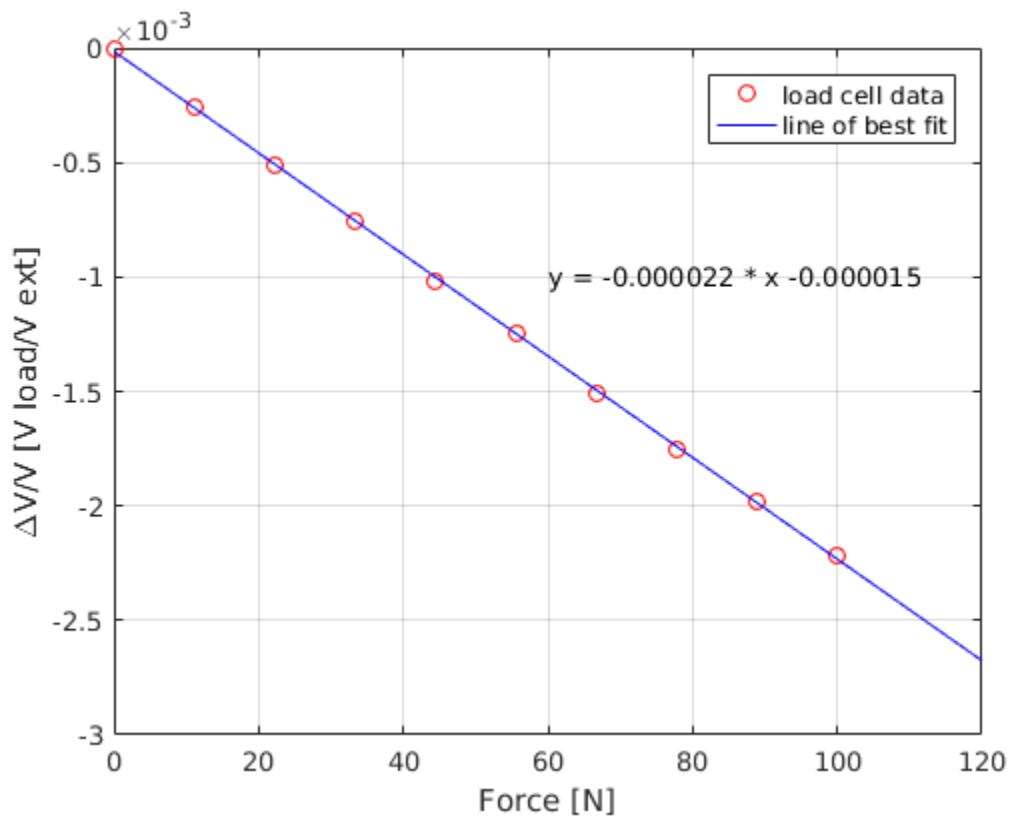


Figure 23. Load Cell Calibration

The Clearpath USV was connected to the calibrated load cell and placed in a water tank to measure various parameters and identify characteristics of the USV.

2. MATLAB and Simulink Setup

MATLAB and Simulink were chosen to implement the high level potential field controller. Figure 24 is a block diagram of the control system and hardware used.

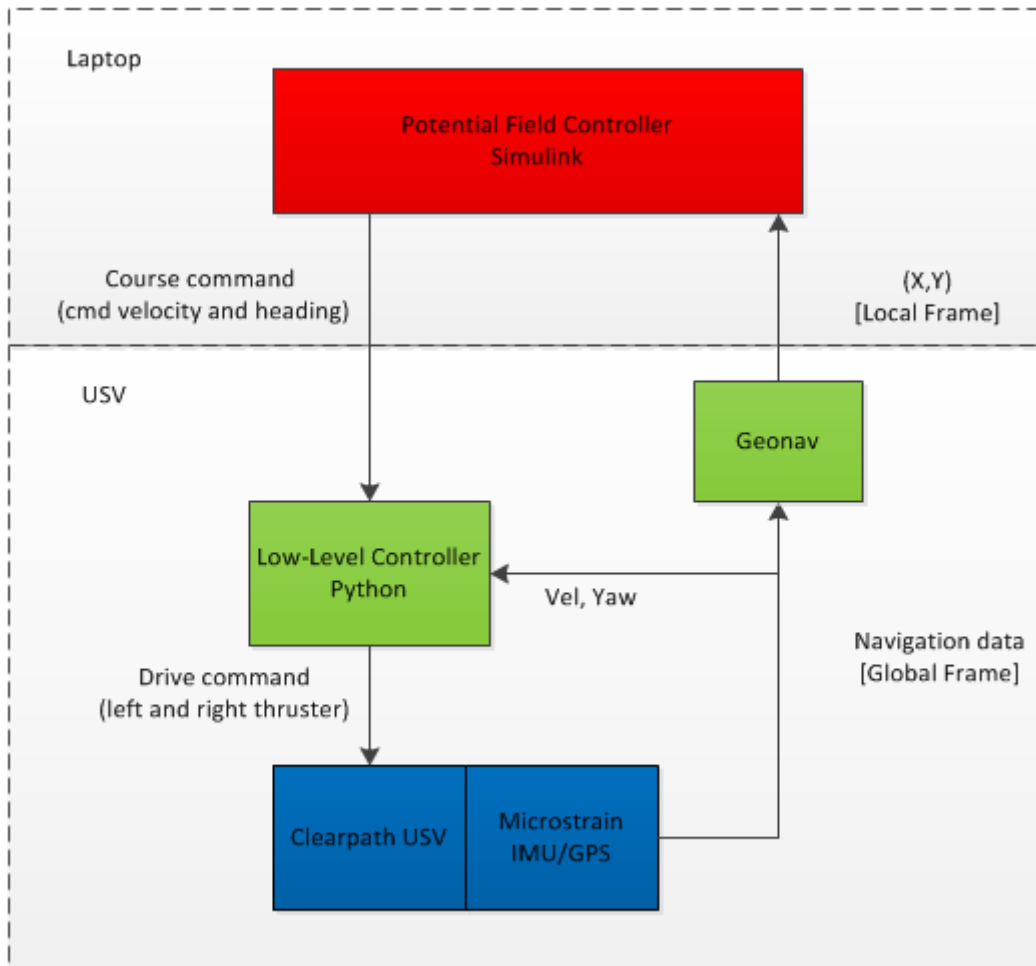


Figure 24. Control System Block Diagram

The course commands are passed via Wi-Fi to the USV where the low-level controller uses the velocity and heading commands as setpoints (goals) for the low-level feedback control. The output of this low-level controller is a drive command for the left and right thrusters. Odometry data (position, velocity,

attitude and attitude-rate) from the micro-strain IMU/GPS is passed back to the low-level controller and potential field controller to complete the feedback loop.

The potential field controller was developed incrementally in the Gazebo simulation environment, presented in Figure 25.

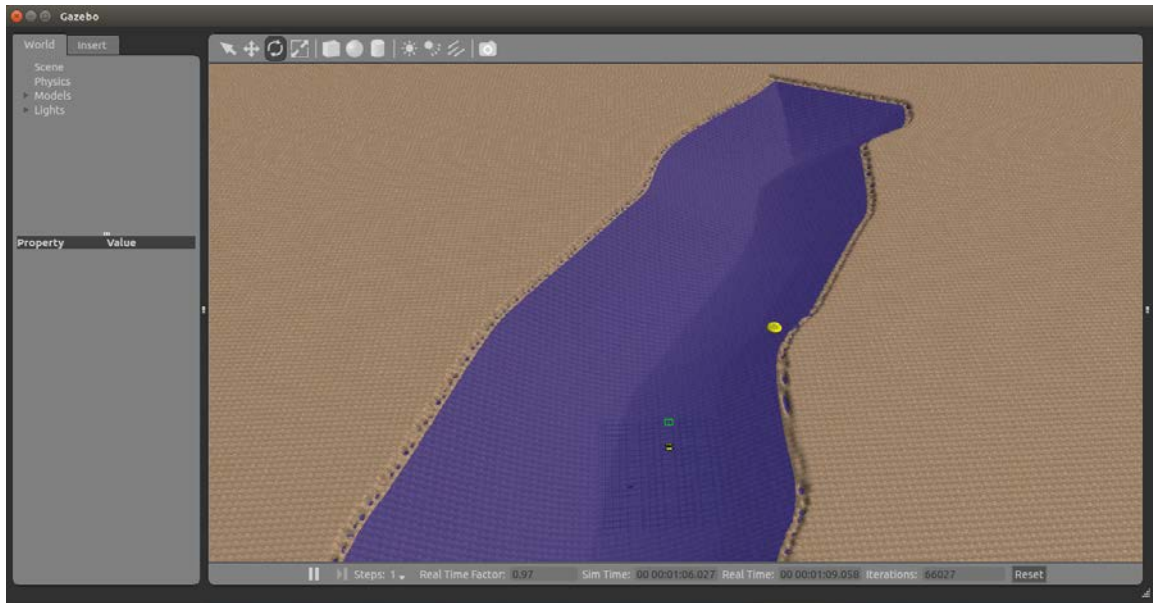


Figure 25. Gazebo Simulation of Lake El Estero

Once the controller worked properly in the simulation then it was tested with the USV at the lake, shown in Figure 26.



Figure 26. Lake El Estero. Adapted from [10].

Adjustments were made at the lake to account for differences in geography between the Gazebo simulations and the lake. The initial controller had one repulsive field, the obstacle, and one attractive field, the target. The basic Simulink model is shown in Figure 27 through Figure 29. Figure 27 shows the ROSNODE block for the position of the USV, the position of the target, and the attractive force inputs. Figure 28 displays the position of the obstacle and the repulsive force inputs. Figure 29 presents the summation of the attractive and repulsive forces, and yaw and speed commands. The yaw and speed commands are passed to the USV through a ROSNODE block. The next increment was adding three obstacles to observe the interaction of the USV and multiple obstacles. The final iteration was creating repulsive potential line fields along the sides of the lake to create a channel with one obstacle and one target. The results are discussed in Sections B and C of this chapter.

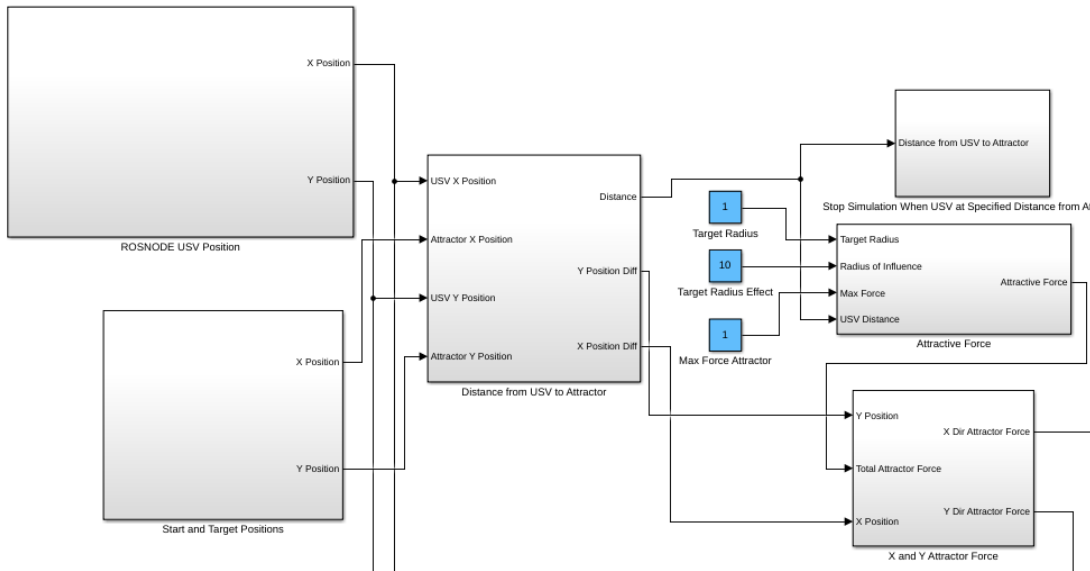


Figure 27. USV Position and Attractive Force in Simulink Model

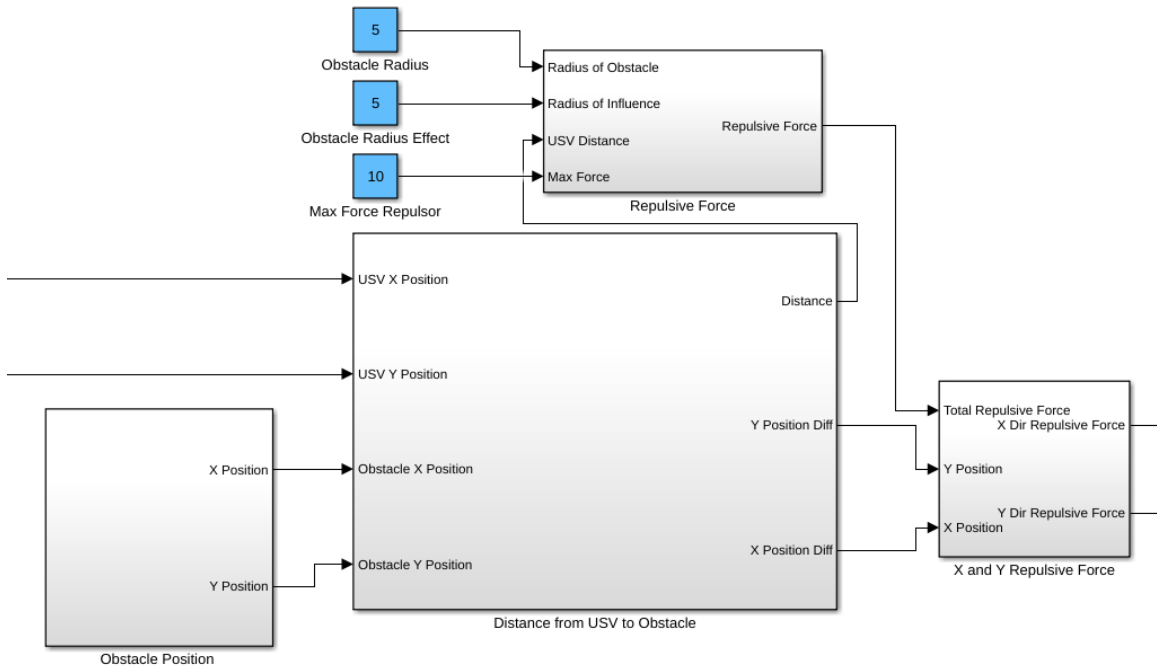


Figure 28. Obstacle and Repulsive Force in Simulink Model

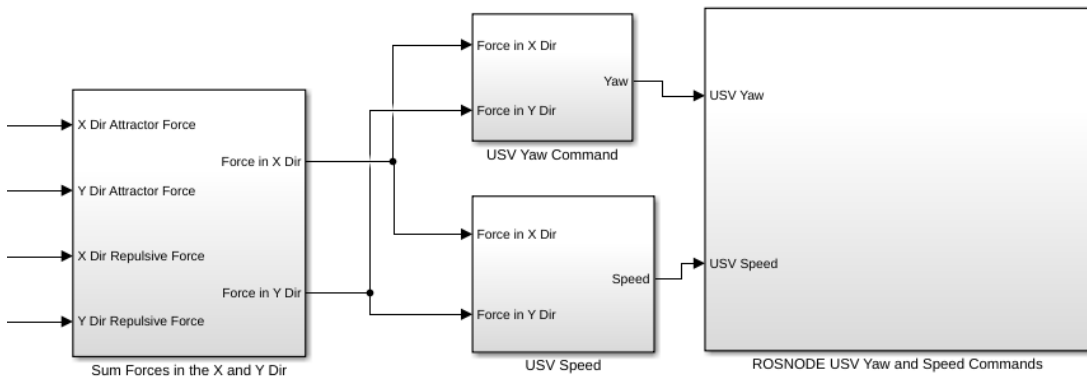


Figure 29. Sum of Forces and Yaw/Speed Commands in Simulink Model

The size of the radius of influence of the obstacle was determined by analyzing the dynamic surge tests. The USV was given the maximum speed command and allowed to reach steady state velocity. The input command was then stopped and the USV decelerated on its own. An assumption was made that

the vehicle would be able to slow down safely before reaching the obstacle based on the time and distance it takes to go from 100% to 10% of maximum speed. The time was measured and the distance to slow down was calculated, approximately 10 meters, by integrating the area underneath the speed curve. The curve is shown in Figure 30.

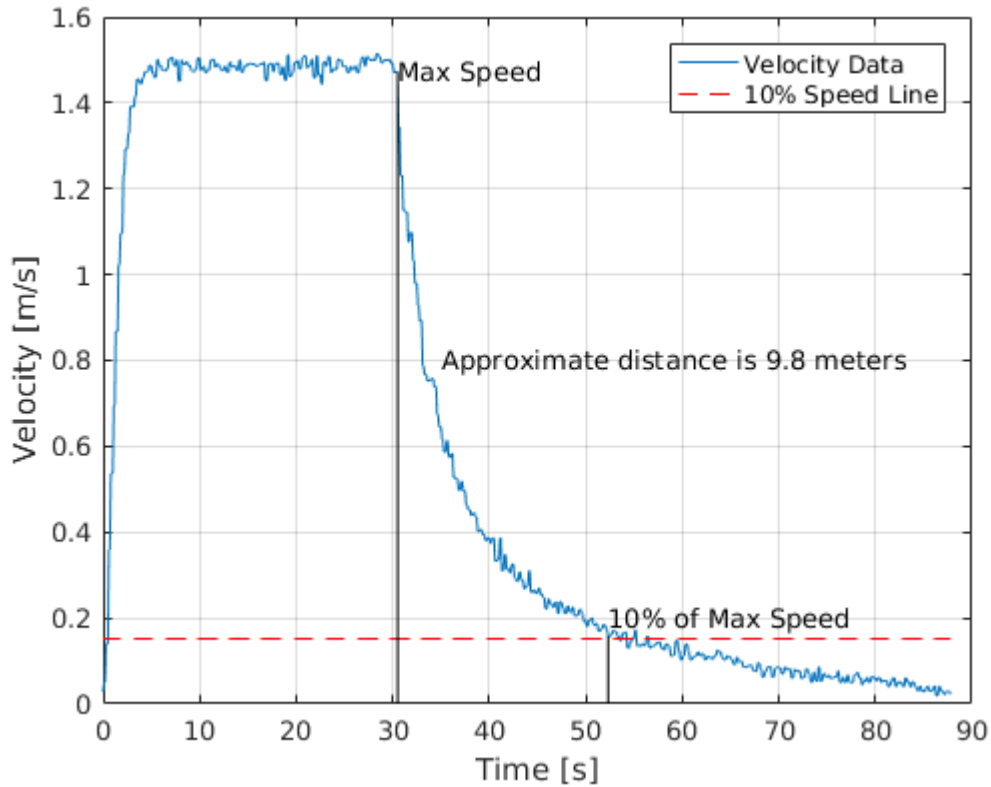


Figure 30. Obstacle Radius of Influence Size

The obstacles in the repulsive potential field line tests have a radius of 10 meters due to the analysis in Figure 30. The MATLAB and Simulink code from the experiments are found in https://gitlab.nps.edu/namanzin/potential_field_NPS_thesis.git.

B. GAZEBO EXPERIMENTAL RESULTS

The initial test in the Gazebo simulation was one obstacle and one target. The USV is travelling toward the top of the plot and its position is plotted in Figure 31. In Figure 31 through Figure 33, the obstacle has an inner radius (solid red circle) of 5 meters and an outer repulsive influence radius (dashed red circle) of 5 meters. The target (dashed green circle) has a radius of 10 meters. Both the obstacle and target have a constant positive gain of 10.

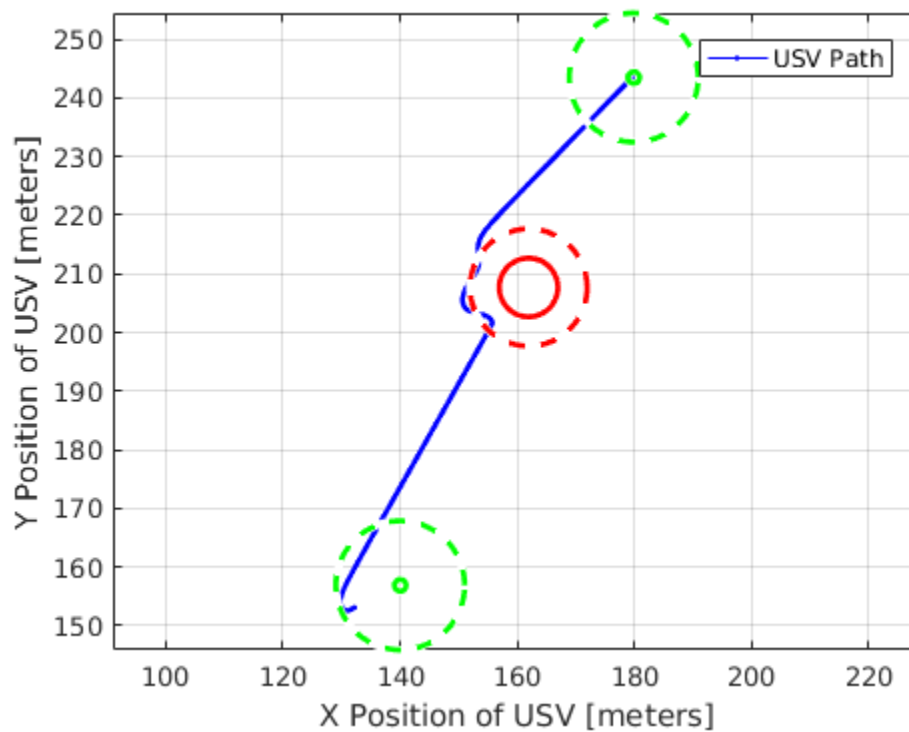


Figure 31. USV Position with One Obstacle in Gazebo

The USV interacts with the attractive potential field in Figure 31 until it crosses the repulsive radius of influence (dashed red circle). The USV maneuvers back and forth across the radius of influence toward the target, where it stops once it crosses the attractive radius of influence (dashed green circle).

The command speed and heading of the USV are plotted in Figure 32. The quiver plot in the figure illustrates the command course data that is being passed to the USV from the potential field controller.

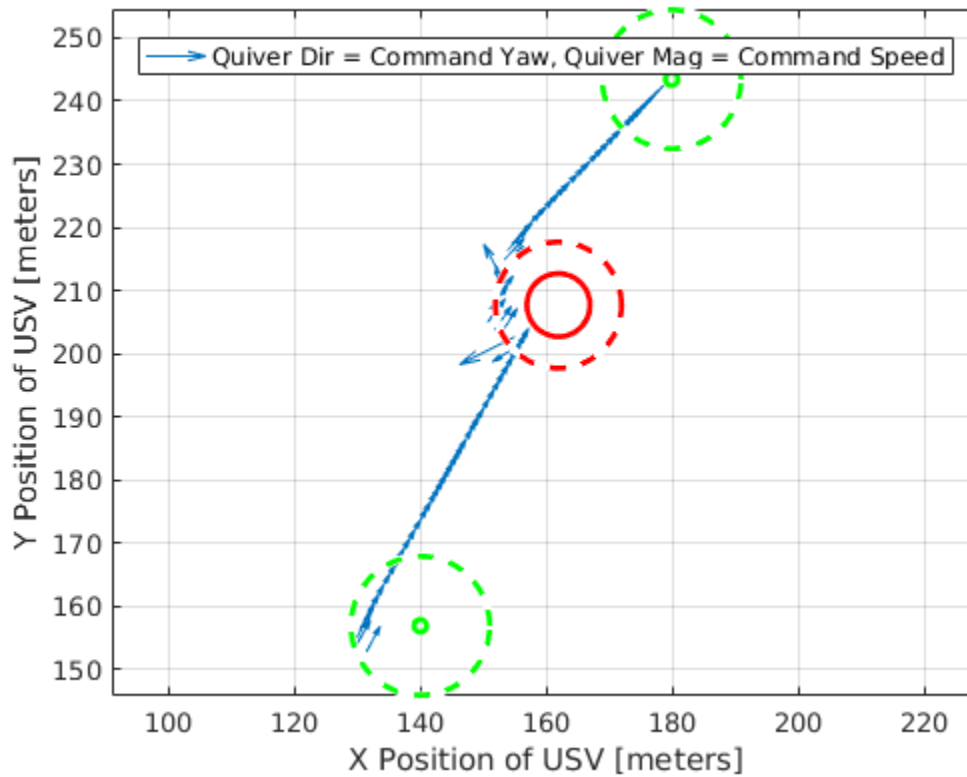


Figure 32. USV Command Yaw and Speed with One Obstacle in Gazebo

Figure 33 displays the speed and heading of USV measured by the simulated IMU in Gazebo. The figure illustrates how the USV converted the commanded yaw and speed into simulated maneuvers to avoid the obstacle and reach the target.

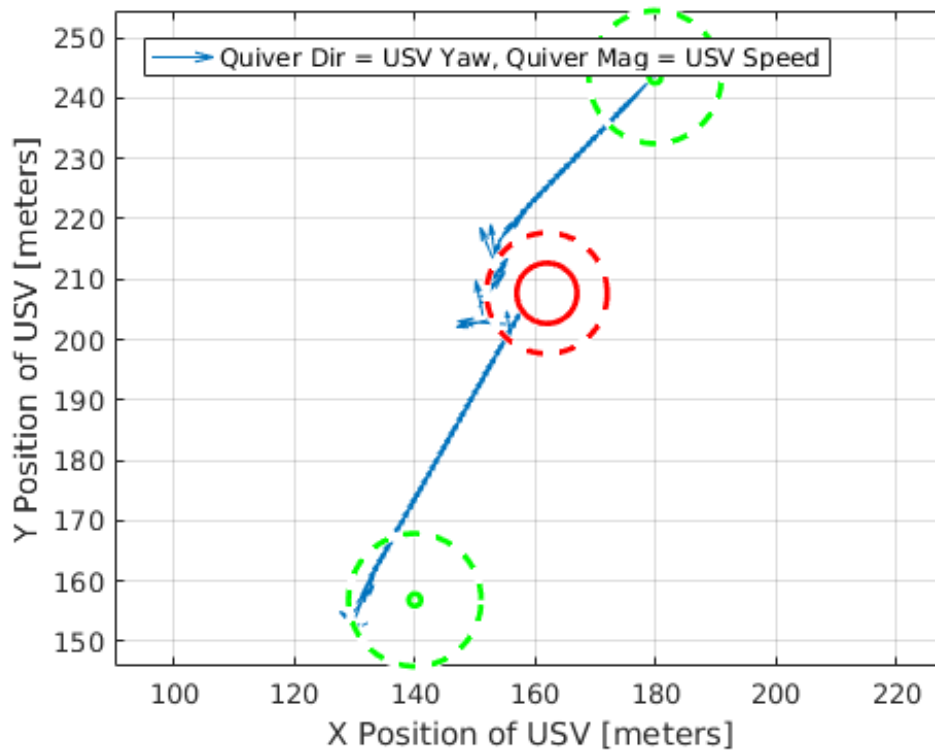


Figure 33. USV Yaw and Speed with One Obstacle in Gazebo

The final test in Gazebo was the USV navigating between a repulsive potential line channel and one obstacle. Figure 34 shows the USV transiting around the obstacle without any interaction with the boundary toward the top of the plot. In Figure 34 through Figure 36, the channel is represented with two solid blue lines. The inner repulsive potential field lines (dashed red line) are 2 meters from the solid blue channel lines. The outer repulsive potential field lines (dashed red line) are 5 meters from the solid blue channel lines. The potential field lines have a constant positive repulsive gain of 10. The middle obstacle has an inner radius (solid red circle) of 1 meter and an outer repulsive influence radius (dashed red circle) of 10 meters. The target (dashed green circle) has an attractive influence radius of 10 meters. The obstacle has a constant positive gain of 10 while the target has a gain of 1.

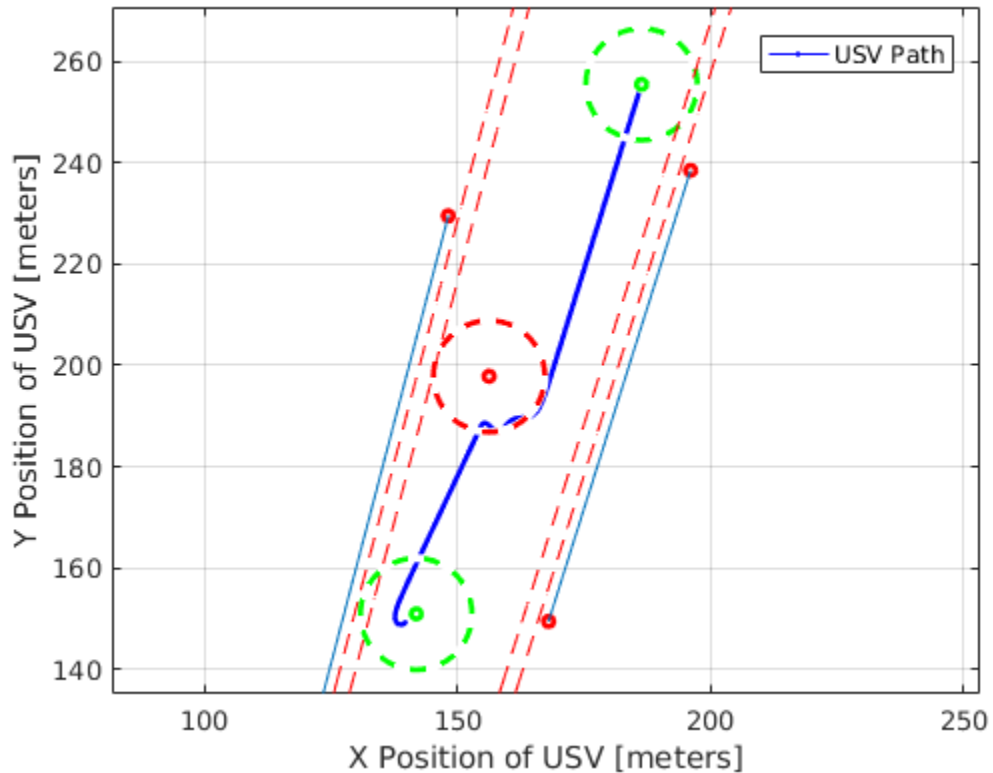


Figure 34. USV Position with Repulsive Channel and One Obstacle in Gazebo

The command speed and heading of the USV are plotted in Figure 35.

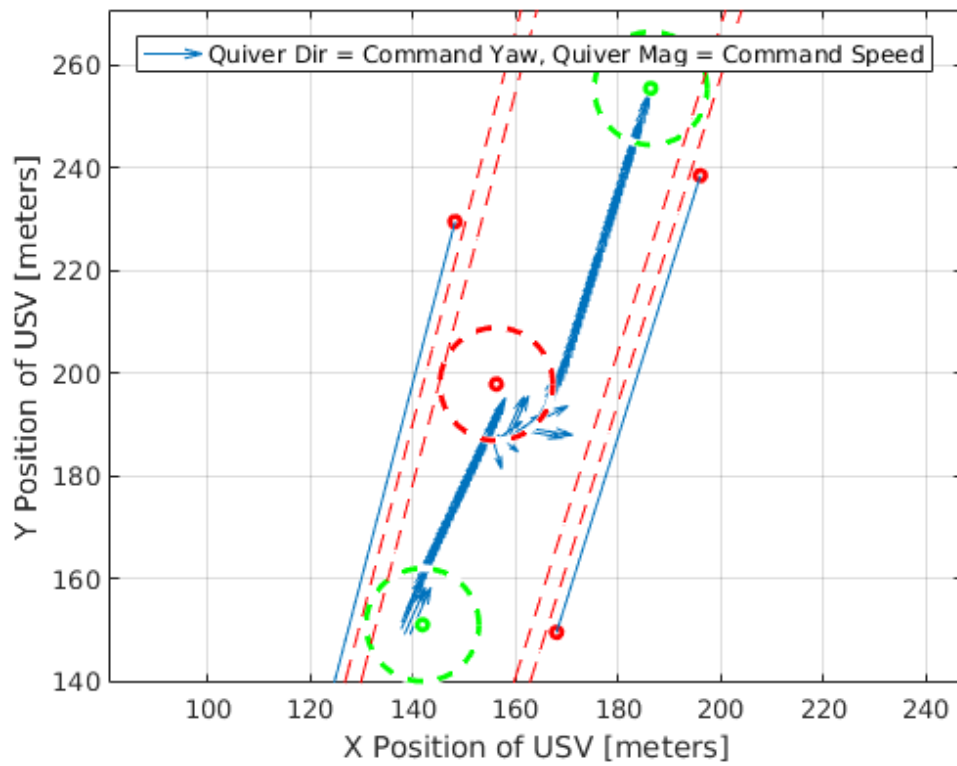


Figure 35. USV Command Yaw and Speed with Repulsive Channel and One Obstacle in Gazebo

In Figure 36, the USV is shown proceeding toward the target, crossing the radius of influence of the obstacle (dashed red circle), and turning in the opposite direction with a large increase in speed. The USV then turns toward the potential line boundary (dashed red line) and maneuvers toward the target (dashed green circle) at the top of the plot.

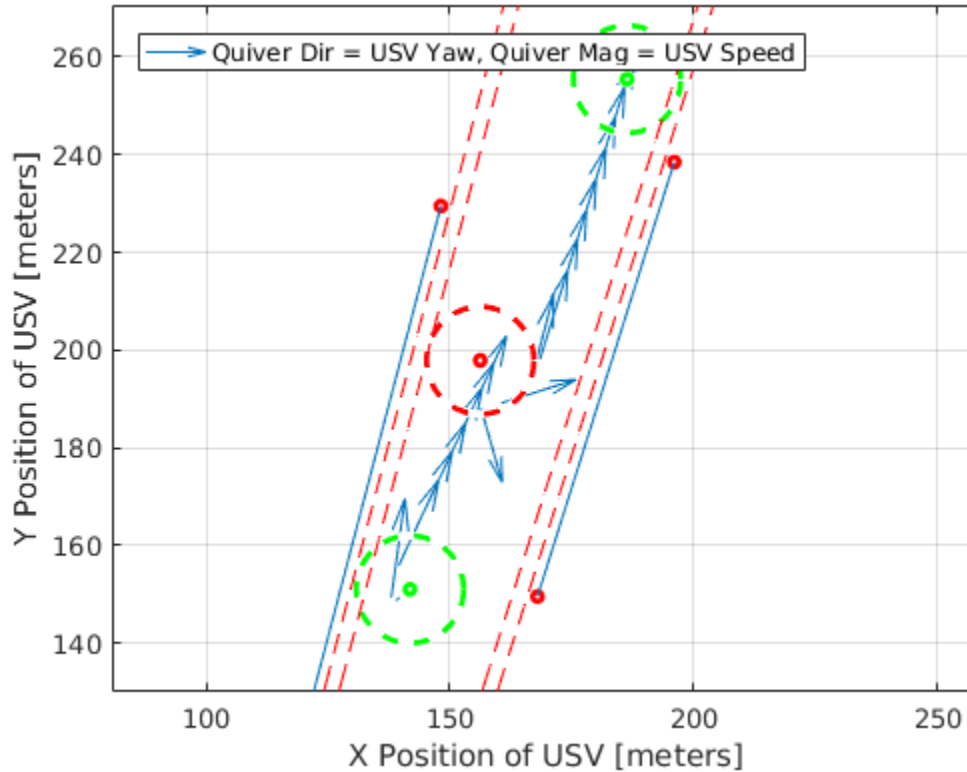


Figure 36. USV Yaw and Speed with Repulsive Channel and One Obstacle in Gazebo

The Gazebo simulations validated that the potential field controller developed in Simulink worked. The follow-on experiment was to integrate the controller with the Kingfisher USV and test it in a real world environment, Lake El Estero. Multiple experiments involving known potential field obstacles and boundary lines were conducted and discussed in Section C.

C. LAKE EL ESTERO EXPERIMENTAL RESULTS

As discussed earlier the initial test was one obstacle and one target. The USV is travelling toward the top of the plot and its position is plotted in Figure 37. In Figure 37 through Figure 39, the obstacle has an inner radius (solid red circle) of 5 meters and an outer repulsive influence radius (dashed red circle) of 5 meters. The target (dashed green circle) has a radius of 10 meters. Both the obstacle and target have a constant positive gain of 10.

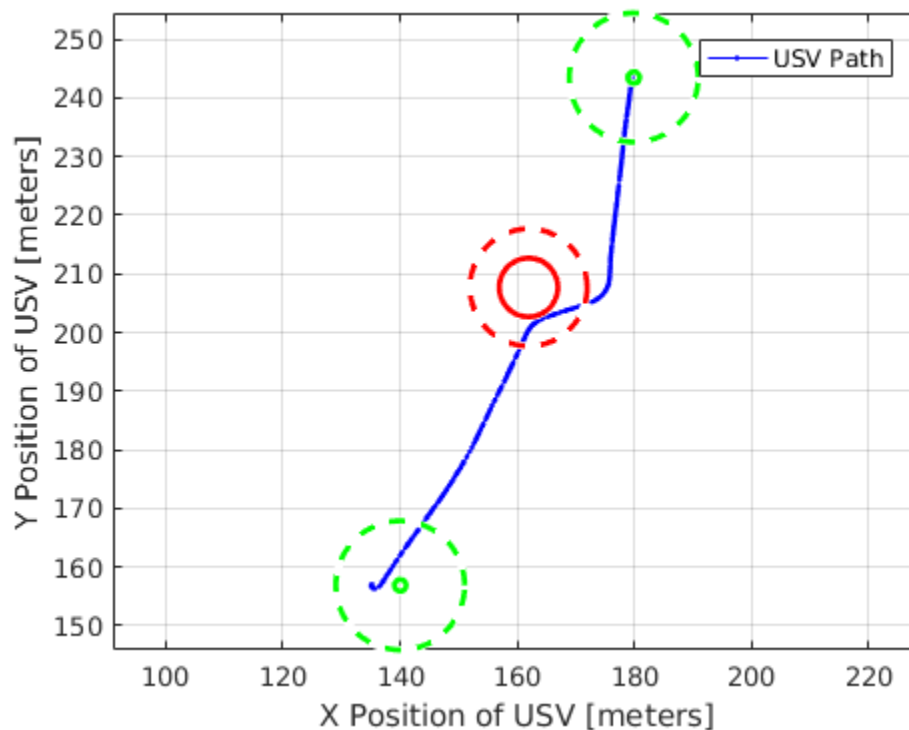


Figure 37. USV Position with One Obstacle

The USV initially only interacts with the attractive potential field in Figure 37 until it crosses the repulsive radius of influence (dashed red circle). The USV maneuvers to exit the radius of influence and continues to the target, where it stops once it crosses the attractive radius of influence (dashed green circle).

The command speed and heading of the USV are plotted in Figure 38. The quiver plot in the figure illustrates the command course data that is being passed to the USV from the potential field controller.

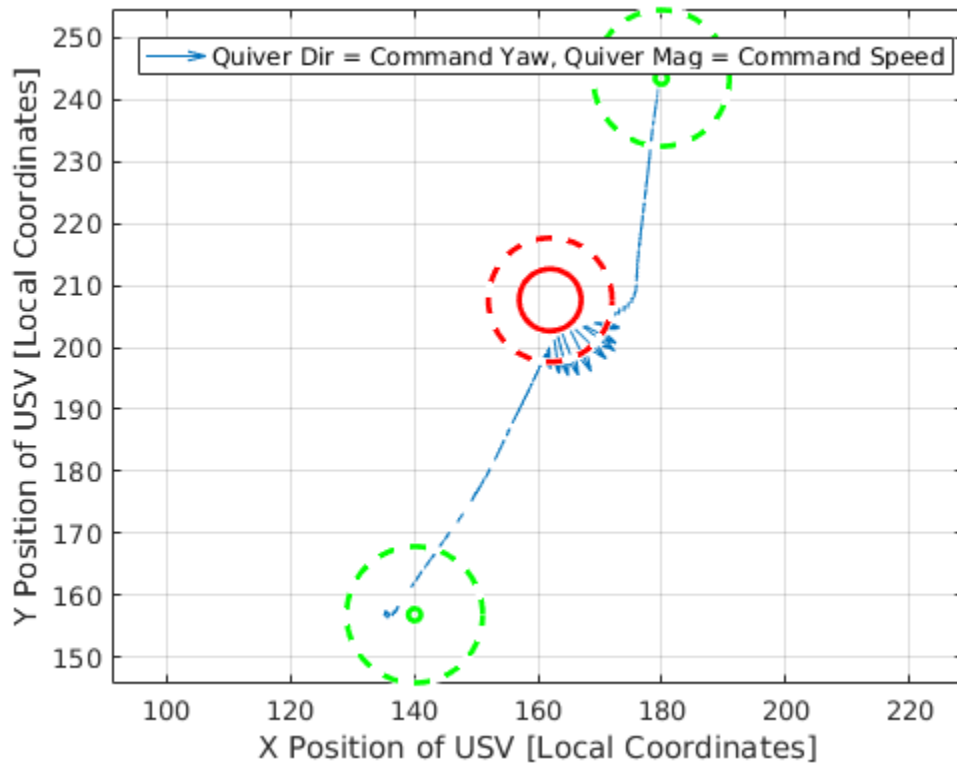


Figure 38. USV Command Yaw and Speed with One Obstacle

Figure 39 displays the speed and heading of the USV measured by the micro-strain IMU/GPS. The figure illustrates how the USV converted the commanded yaw and speed into real-world maneuvers to avoid the obstacle and reach the target.

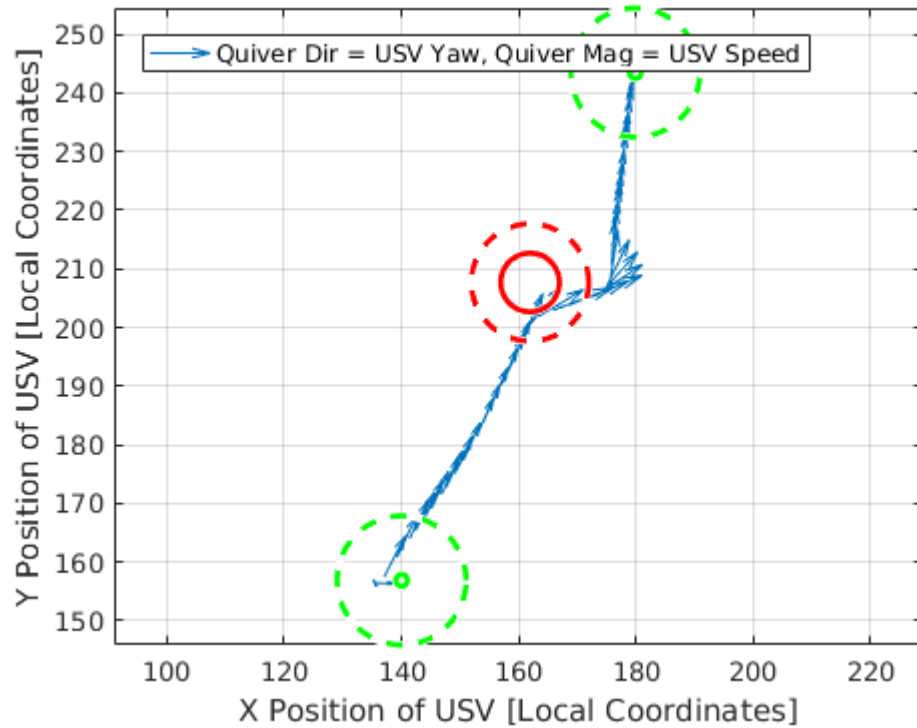


Figure 39. USV Yaw and Speed with One Obstacle

The next test was implementing three obstacles and one target. The USV is travelling toward the top of the plot and its position is plotted in Figure 40. In Figure 40 through Figure 42, the two smaller obstacles have an inner radius (solid red circle) of 1 meter and an outer repulsive influence radius (dashed red circle) of 5 meters. The middle obstacle has an inner radius (solid red circle) of 5 meters and an outer repulsive influence radius (dashed red circle) of 5 meters. The target (dashed green circle) has a radius of 10 meters. Both the obstacles and target have a constant positive gain of 10.

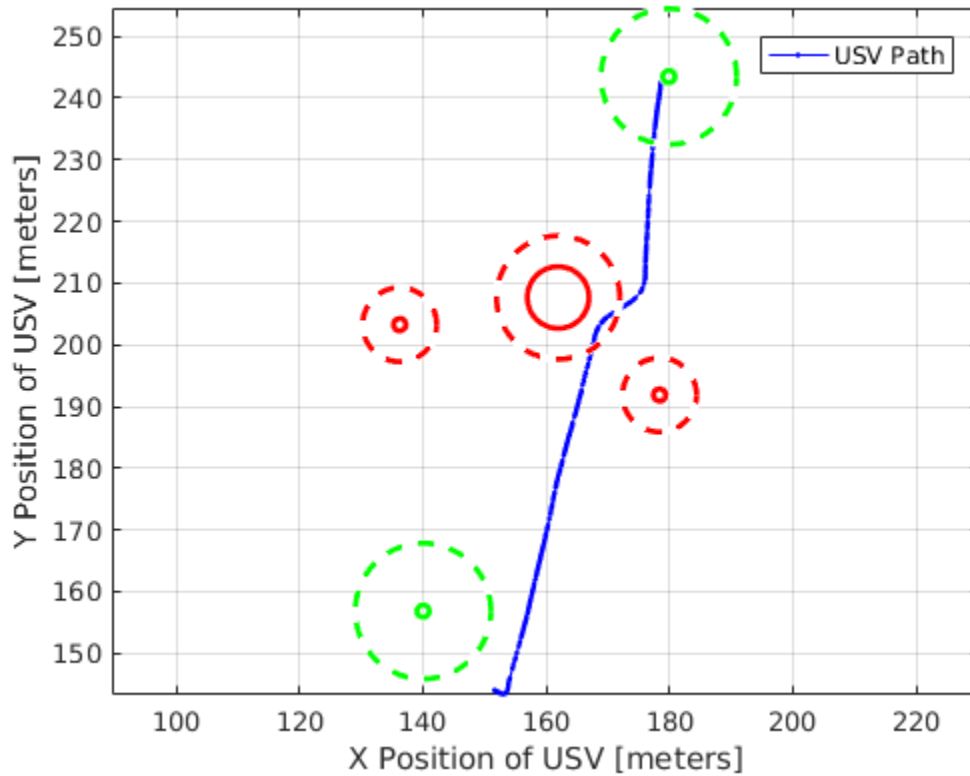


Figure 40. USV Position with Three Obstacles

The USV only interacts with the large middle obstacle while transiting toward the target. The command speed and heading of the USV are plotted in Figure 41.

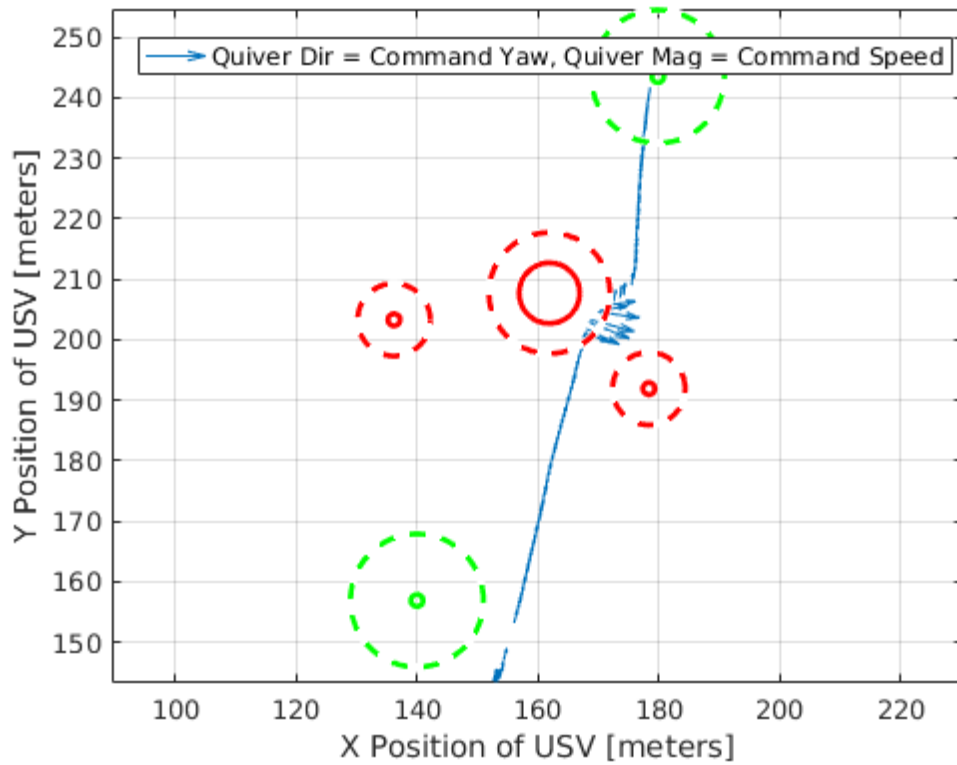


Figure 41. USV Command Yaw and Speed with Three Obstacles

Figure 42 displays the speed and heading of the USV measured by the micro-strain IMU/GPS. The figure once again illustrates how the USV converted the commanded yaw and speed into real-world maneuvers to avoid the obstacles and reach the target.

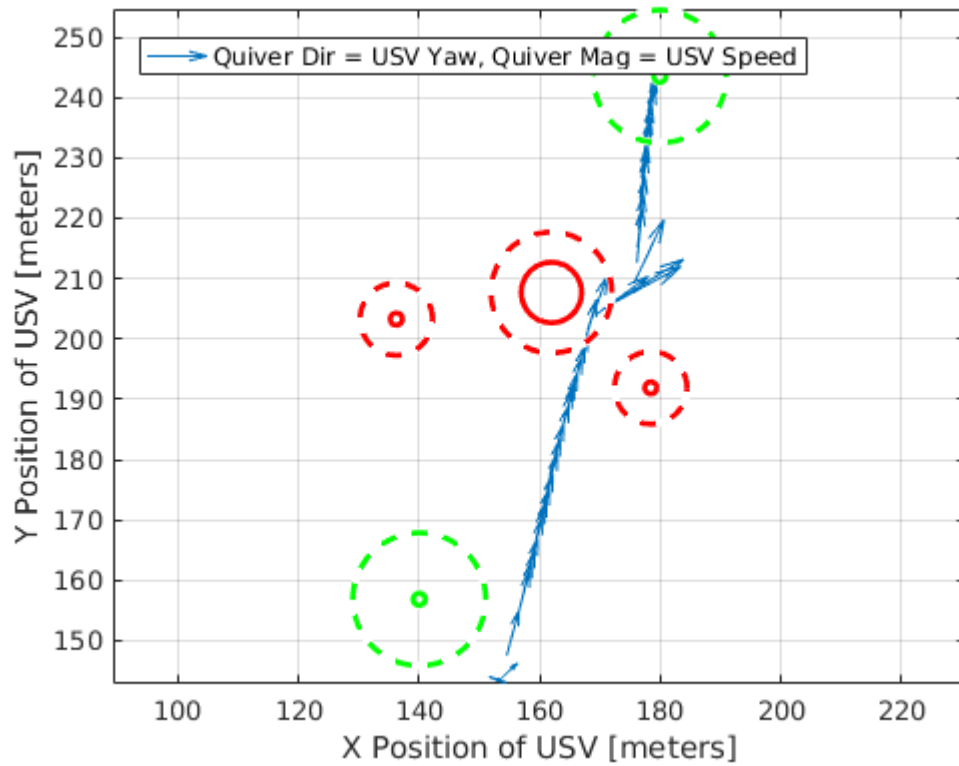


Figure 42. USV Yaw and Speed with Three Obstacles

The next test was a return trip of the USV between the three obstacles. The previous starting position is now the target and the USV is travelling toward the bottom of the plot in Figure 43. In Figure 43 through Figure 45, the two smaller obstacles have an inner radius (solid red circle) of 1 meter and an outer repulsive influence radius (dashed red circle) of 5 meters. The middle obstacle has an inner radius (solid red circle) of 5 meters and an outer repulsive influence radius (dashed red circle) of 5 meters. The target (dashed green circle) has a radius of 10 meters. Both the obstacles and target have a constant positive gain of 10.

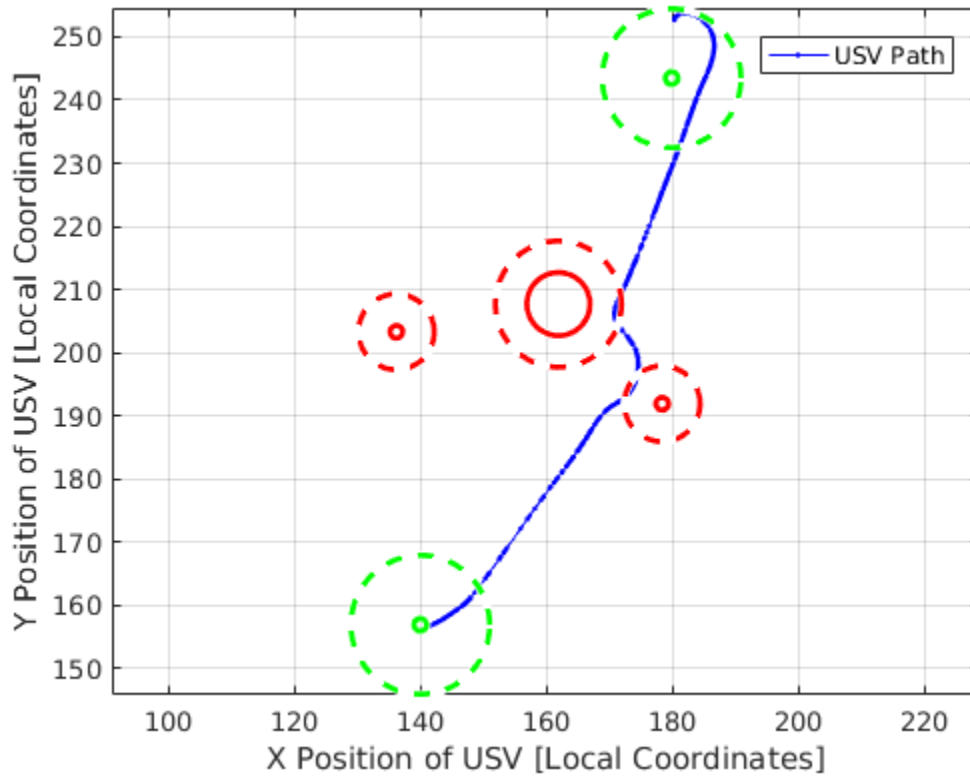


Figure 43. USV Return Trip with Three Obstacles

The USV crosses the middle obstacle's radius of influence (dashed red circle) and turns toward the smaller obstacle. The USV then interacts with the repulsive field of the smaller boundary (dashed red circle) and turns toward the target to complete the test. The command speed and heading of the USV are plotted in Figure 44.

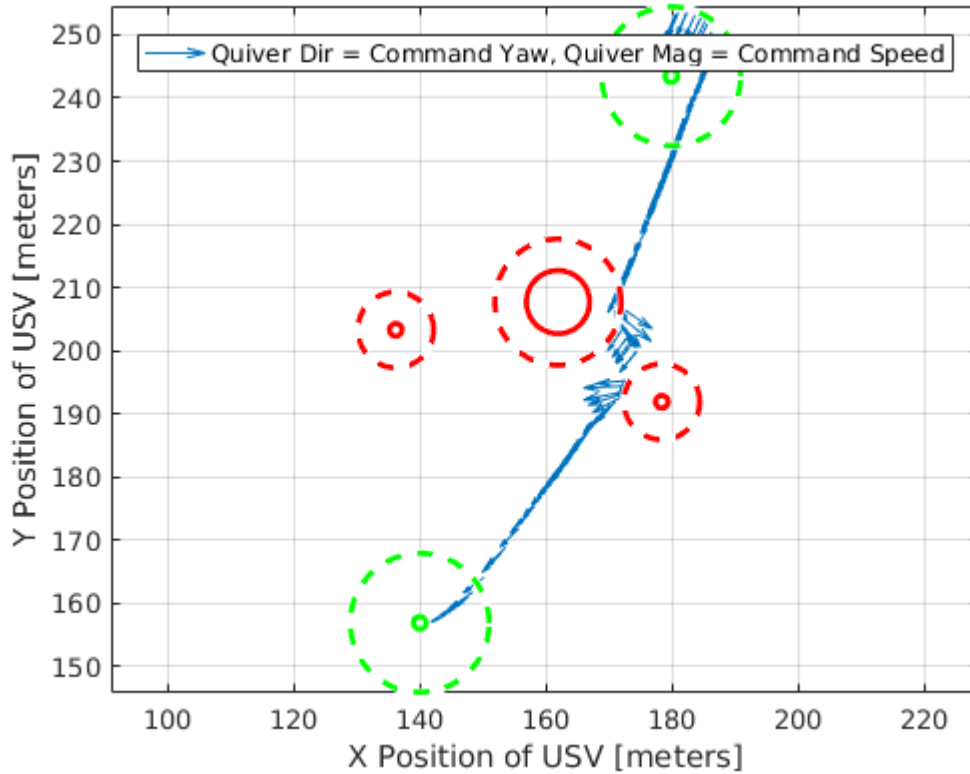


Figure 44. USV Command Yaw and Speed with Three Obstacles

Figure 45 displays the speed and heading of the USV's return trip measured by the micro-strain IMU/GPS. The most noticeable aspect of the quiver plot is the increase in the size of the arrows, the USV speed, when the USV exits the radius of influence (dashed red circle) of both obstacles.

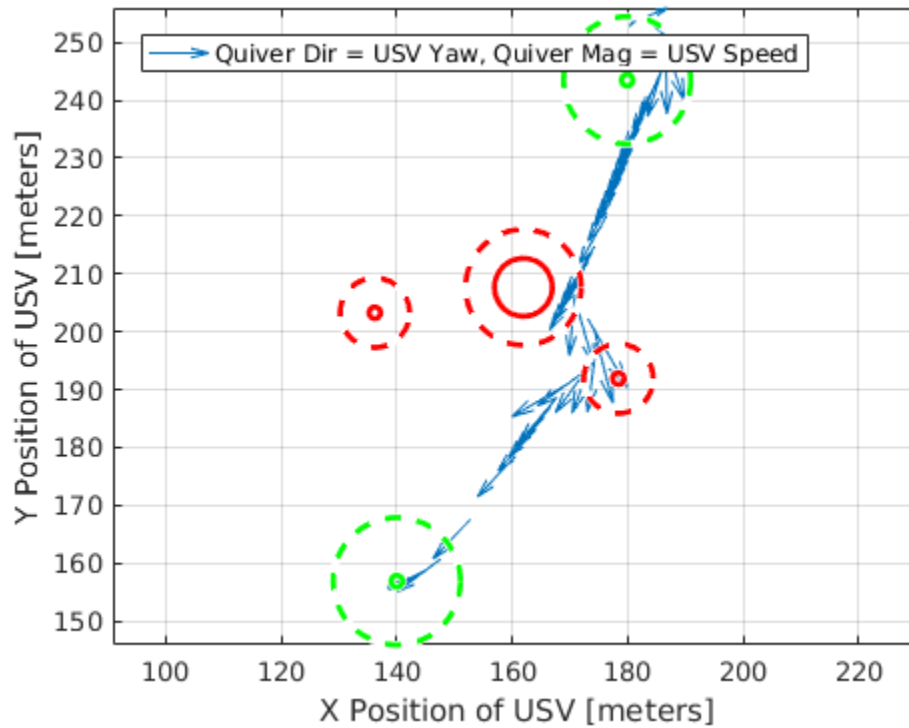


Figure 45. USV Yaw and Speed with Three Obstacles

The final test was the USV navigating between a repulsive potential line channel and one obstacle. Figure 46 shows the USV transiting toward the top of the plot without any interaction with the channel. In Figure 46 through Figure 48, the channel is represented with two solid blue lines. The inner repulsive potential field lines (dashed red line) are 2 meters from the solid blue channel lines. The outer repulsive potential field lines (dashed red line) are 5 meters from the solid blue channel lines. The potential field lines have a constant positive repulsive gain of 10. The middle obstacle has an inner radius (solid red circle) of 1 meter and an outer repulsive influence radius (dashed red circle) of 10 meters. The target (dashed green circle) has an attractive influence radius of 10 meters. The obstacle has a constant positive gain of 10 while the target has a gain of 1.

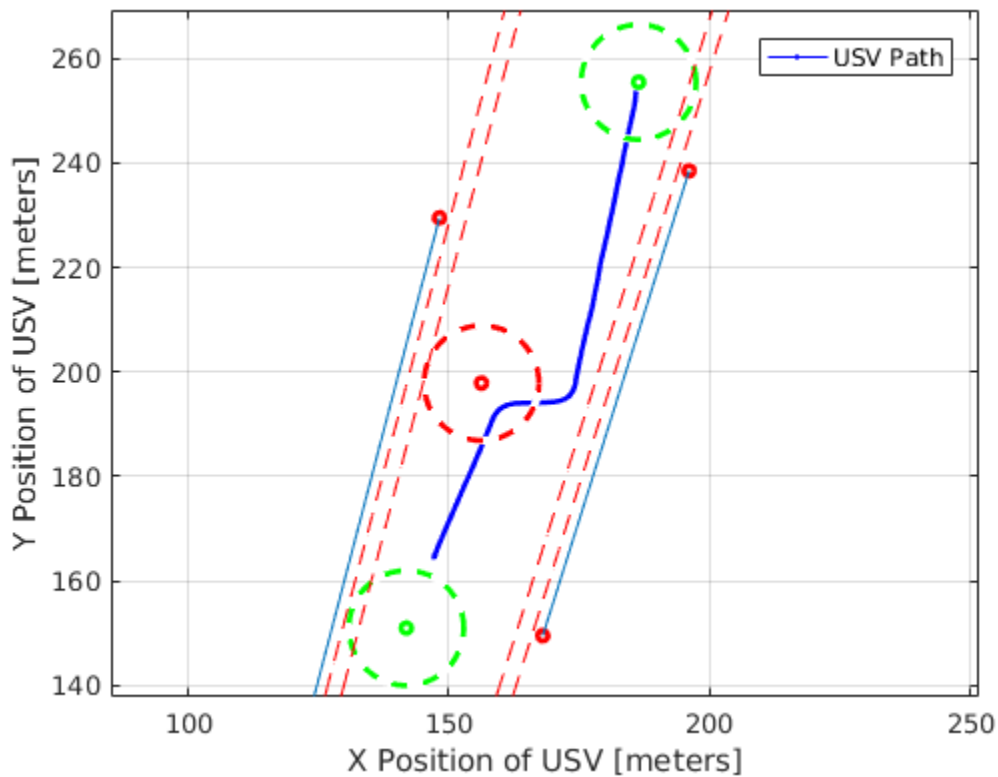


Figure 46. USV Position with Repulsive Channel and One Obstacle

The command speed and heading of the USV are plotted in Figure 47.

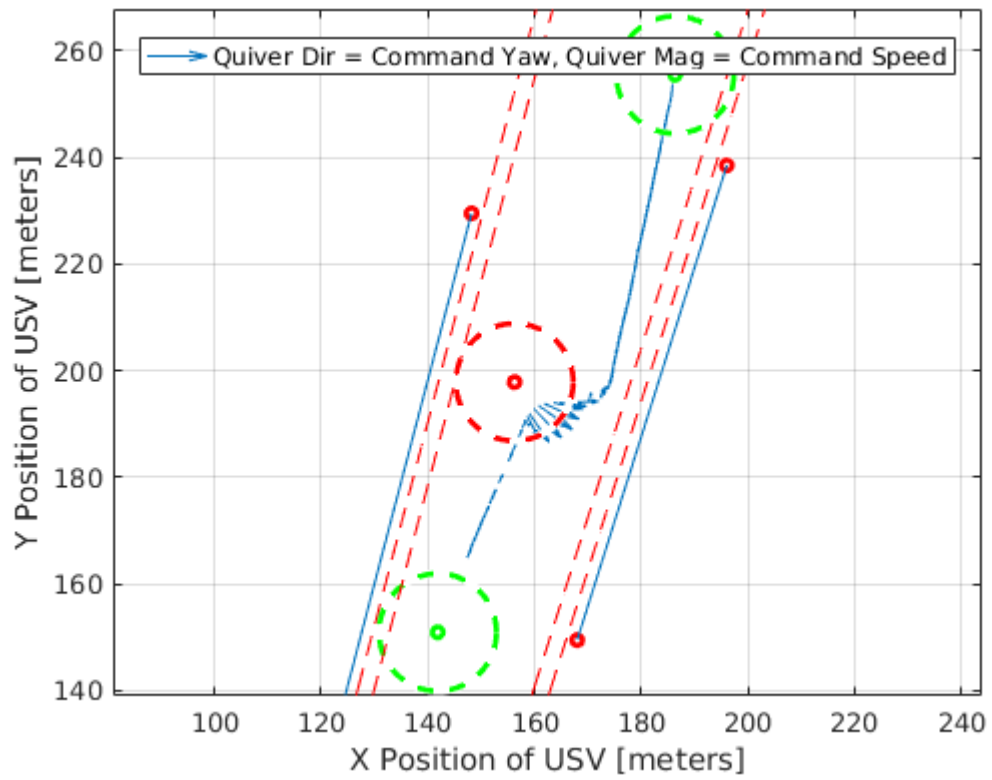


Figure 47. USV Command Yaw and Speed with Repulsive Channel and One Obstacle

Figure 48 displays the speed and heading of the USV's trip measured by the micro-strain IMU/GPS.

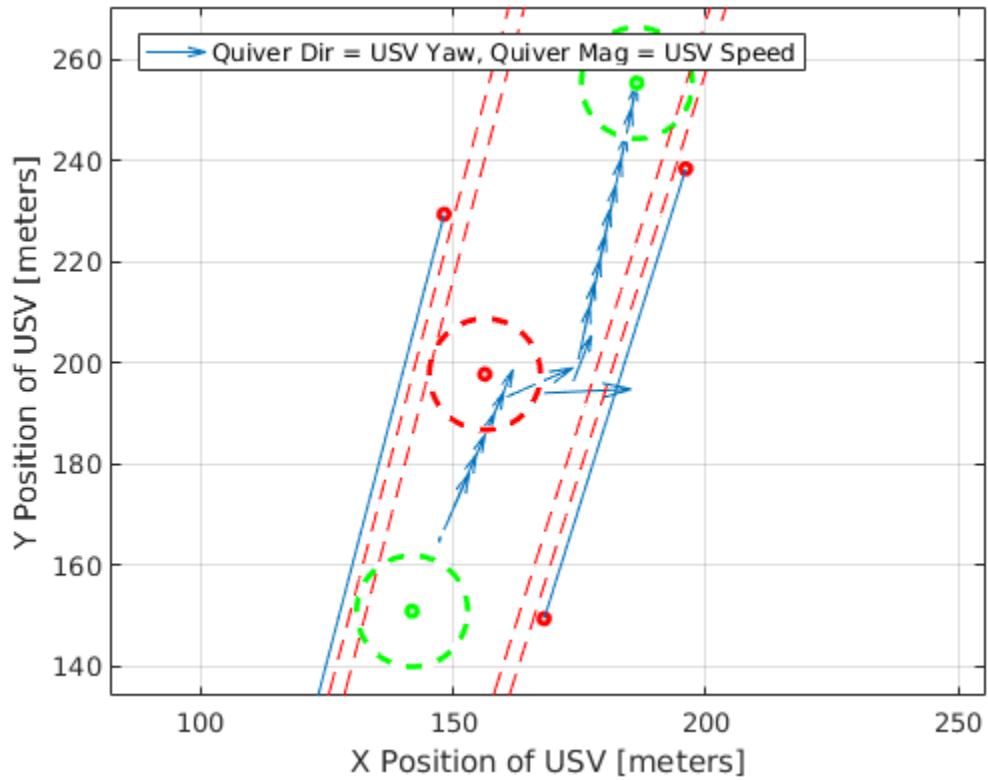


Figure 48. USV Yaw and Speed with Repulsive Channel and One Obstacle

In Figure 49, the USV is shown starting inside the repulsive potential line channel and moving toward the target at the top of the plot. In Figure 49 through Figure 51, the channel is represented with two solid blue lines. The inner repulsive potential field lines (dashed red line) are 2 meters from the solid blue channel lines. The outer repulsive potential field lines (dashed red line) are 5 meters from the solid blue channel lines. The potential field lines have a constant positive repulsive gain of 10. The middle obstacle has an inner radius (solid red circle) of 1 meter and an outer repulsive influence radius (dashed red circle) of 10 meters. The target (dashed green circle) has an attractive influence radius of 10 meters. The obstacle has a constant positive gain of 5 while the target has a gain of 1. The USV is repelled by the channel potential field (dashed red line) and only interacts with the attractive target field until it crosses the obstacle's repulsive radius of influence (dashed red circle). The USV then exits the obstacle and continues on its track toward the target.

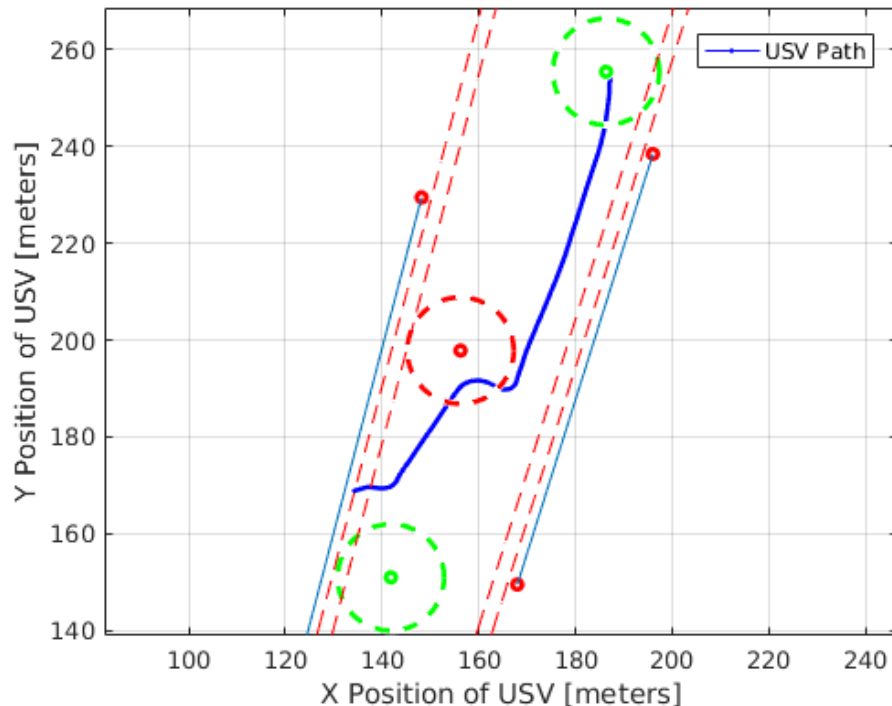


Figure 49. USV Position with Repulsive Channel and One Obstacle

The command speed and heading of the USV are plotted in Figure 50. The commanded speed and direction are approximately perpendicular to the repulsive potential field line (dashed red line) in the figure. The repulsive field forces the USV to exit the boundary toward the middle of the channel. The USV then begins to turn toward the attractive field of the target until it maneuvers around the obstacle (dashed red circle) to reach the goal (dashed green circle).

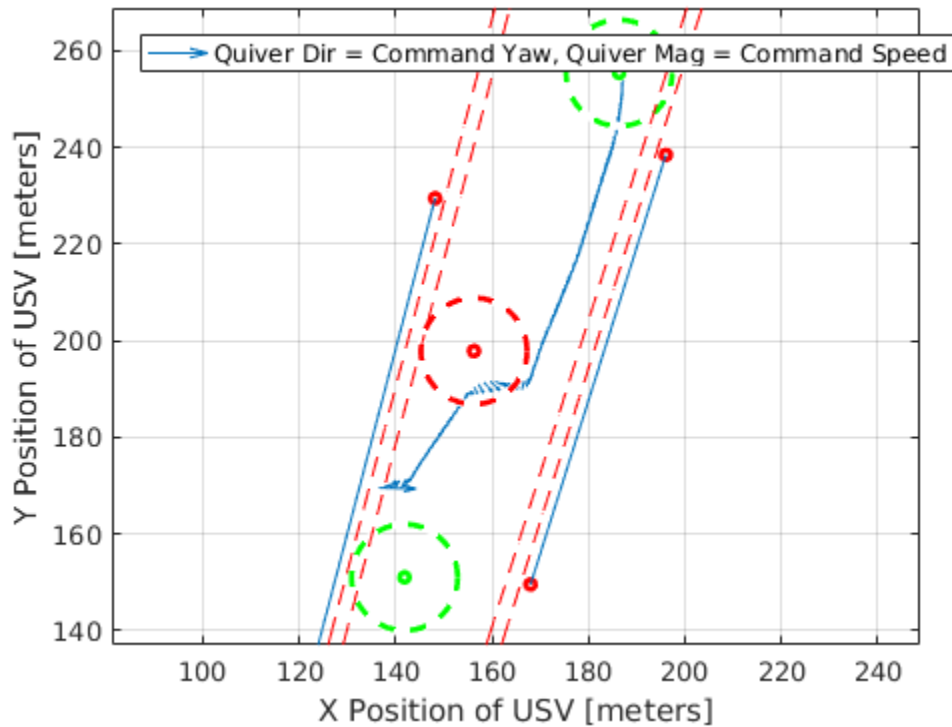


Figure 50. USV Command Yaw and Speed with Repulsive Channel and One Obstacle

Figure 51 displays the speed and heading of the USV's trip measured by the micro-strain IMU/GPS. Once again, the largest speeds of the USV are when it is exiting a repulsive field boundary (dashed red line) and the obstacle (dashed red circle). Upon exiting the obstacle, the yaw of the USV turns toward the target (dashed green circle) due to the attractive potential field.

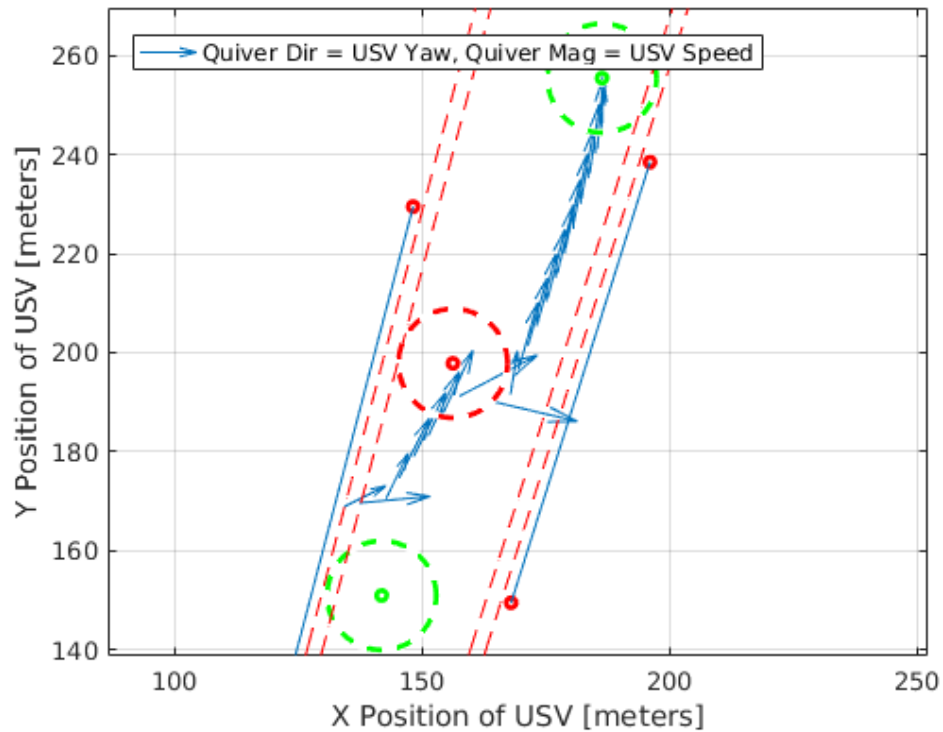


Figure 51. USV Yaw and Speed with Repulsive Channel and One Obstacle

The next test was a return trip of the USV between the channel and the boundary. The previous starting position is now the target and the USV is travelling toward the bottom of the plot in Figure 52. In Figure 52 through Figure 54, the channel is represented with two solid blue lines. The inner repulsive potential field lines (dashed red line) are 2 meters from the solid blue channel lines. The outer repulsive potential field lines (dashed red line) are 5 meters from the solid blue channel lines. The potential field lines have a constant positive repulsive gain of 10. The middle obstacle has an inner radius (solid red circle) of 1 meter and an outer repulsive influence radius (dashed red circle) of 10 meters. The target (dashed green circle) has an attractive influence radius of 10 meters. The obstacle has a constant positive gain of 5 while the target has a gain of 1. The USV navigates between the obstacle (dashed red circle) and the potential line channel (dashed red lines) while transiting to the target. Both the attractive and repulsive fields interact appropriately with the USV. The repulsive field of the potential lines force the USV out of the boundary and the attractive field of the target (dashed green circle) draws the USV toward it.

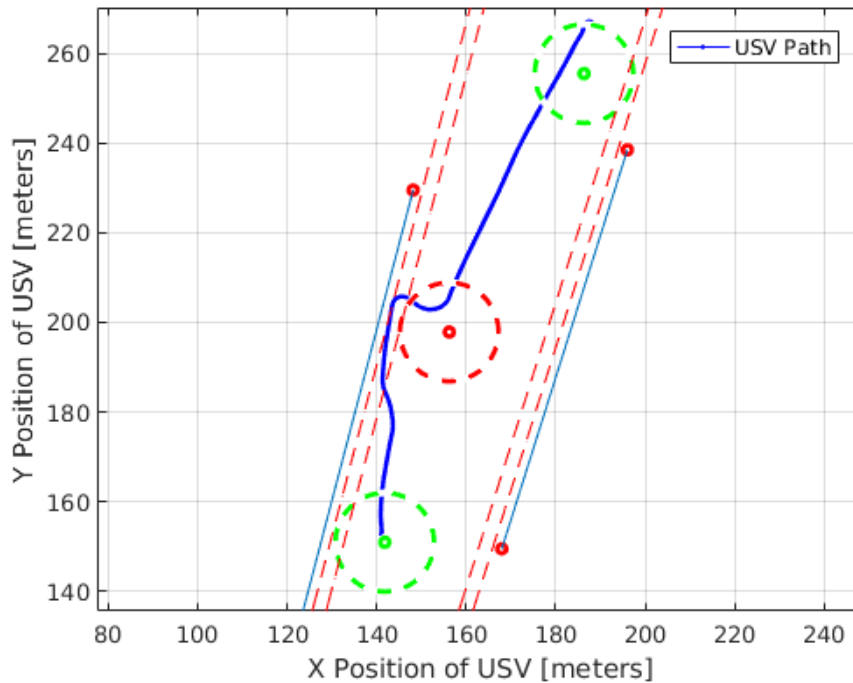


Figure 52. USV Return Trip with Repulsive Channel and One Obstacle

The command speed and heading of the USV are plotted in Figure 53.

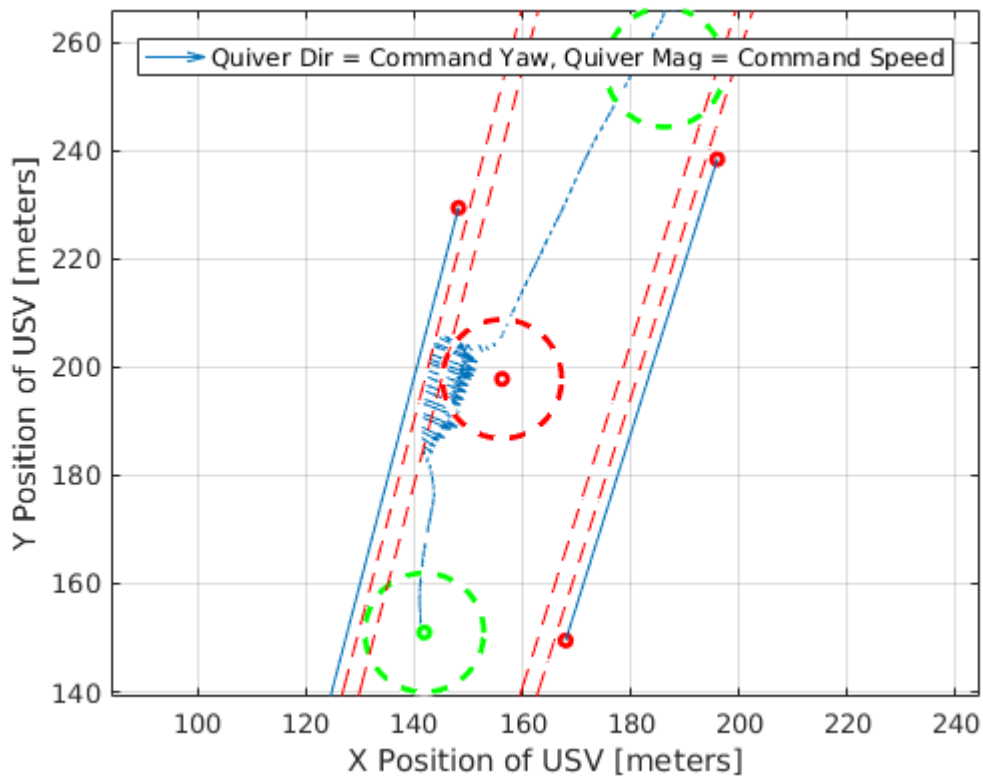


Figure 53. USV Command Yaw and Speed with Repulsive Channel and One Obstacle

The repulsive forces of the potential line are perpendicular to the boundary (dashed red lines) and direct the USV toward the obstacle (dashed red circle), but are minimized due to the opposing forces of the obstacle.

Figure 54 displays the speed and heading of the USV's return trip measured by the micro-strain IMU/GPS. The USV enters the middle obstacle (dashed red circle) and turns nearly perpendicular to exit it. The USV then points directly into the potential line boundary (dashed red lines) in Figure 54. Inside the boundary, the USV turns toward the target (dashed green circle) and speeds up to exit the repulsive potential line. The potential field controller and the USV all perform as expected to ensure the USV maneuvers away from repulsive potential fields and toward the attractive potential field.

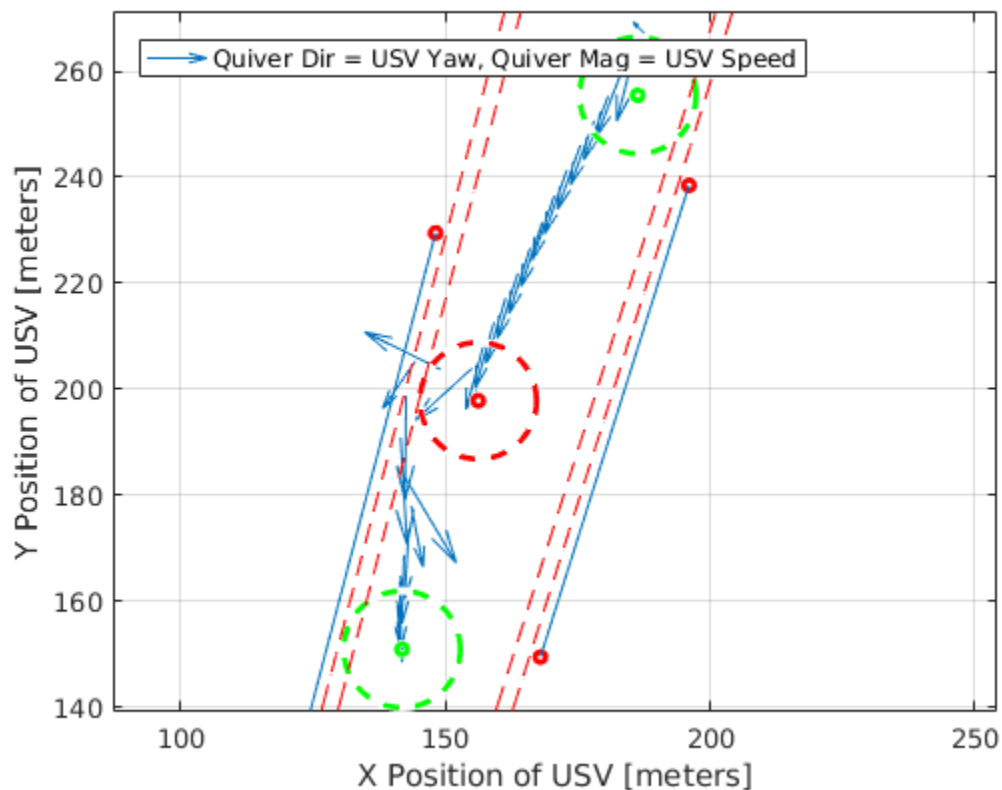


Figure 54. USV Yaw and Speed with Repulsive Channel and One Obstacle

D. COMPARISON OF GAZEBO AND LAKE EL ESTERO RESULTS

The USV tracks from the Gazebo simulations and Lake El Estero experiments were plotted together to compare the differences between the simulated and actual USV. Figure 55 presents the experiment with one obstacle and is a combination of Figure 31 and Figure 37.

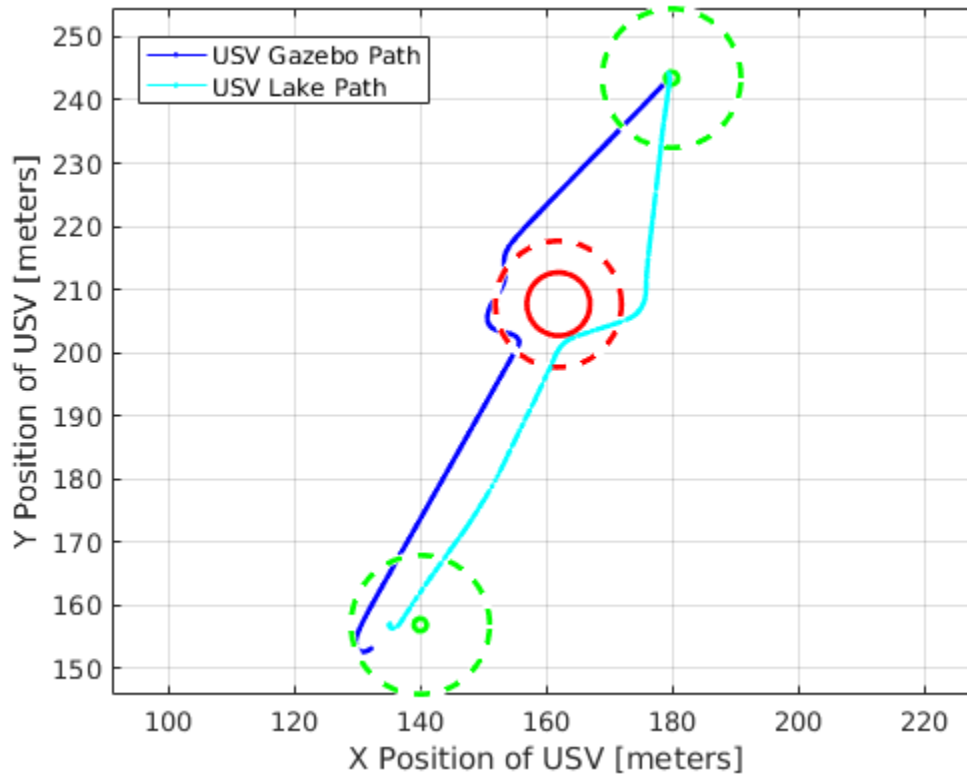


Figure 55. Combined USV Plots with One Obstacle

The USVs begin the experiment transiting toward the attractive potential field in the same direction. The simulated USV (dark blue line) reacts immediately with the repulsive potential field obstacle and continues to interact with it while maneuvering to the left. The real world USV (light blue line) requires more time and space to react to the obstacle. The momentum of the USV requires a larger repulsive force to change directions and speed to avoid the obstacle. The USV exits the obstacle's field of influence (dashed red circle) and

turns toward the target (dashed green circle) to complete the run. The major difference between the two experiments was the interaction with the obstacle and the direction of steering around it.

Figure 56 combines Figure 34 and Figure 46 to show the differences of the USVs navigating between a repulsive potential line channel and one obstacle.

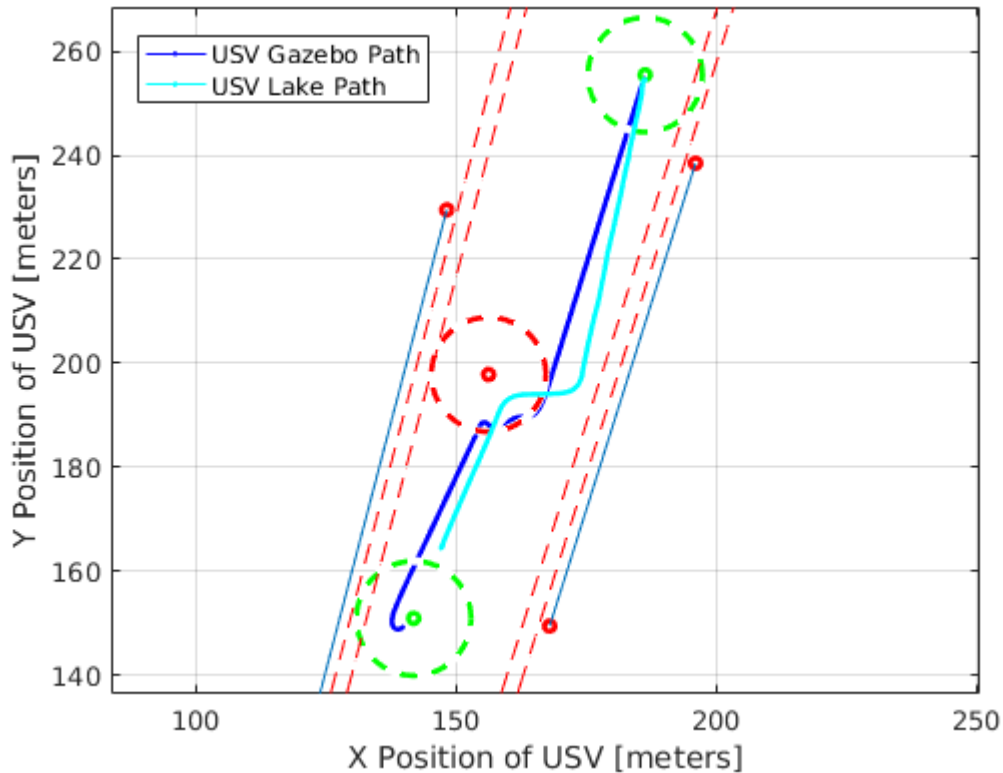


Figure 56. Combined USV Plots with Repulsive Channel and One Obstacle

Once again, both USVs proceeded toward the attractive potential field in the same direction. The simulated USV (dark blue line) interacted consistently with the obstacle (dashed red circle) to steer around it. The real world USV (light blue line) required a larger repulsive force similar to Figure 55 to avoid the obstacle. The real world USV exited the radius of influence nearly perpendicular

with a large direction and speed change. Neither USV interacted with the potential line boundaries during the experiment.

V. CONCLUSION

A. SUMMARY OF RESULTS

A piecewise linear potential field model was implemented on the Clearpath USV using MATLAB and Simulink. The dynamics of the USV were measured and tested to create a suitable model in the Gazebo simulation environment. The USV model and piecewise linear potential field model were tested in Gazebo and in the field. For this research, the location of all obstacles was provided to the USV a priori. The simulations and field experiments were compared to evaluate the performance of the USV and potential field algorithm. The qualitative results show that the simulation, using the USV maneuvering model, captures the important dynamics of the USV and that the unavoidable differences between simulation and experiment require some additional tuning of the algorithm parameters in the field.

Due to the large, nonrestrictive test area, there were no cases of the USV reaching a local minimum and becoming stuck [4]. The USV interacted with the piecewise linear potential fields in a consistent and expected manner. The repulsive fields forced the USV to change direction and speed to exit the obstacles and boundaries. The attractive field would draw the USV quickly and directly to the target. The interaction between the repulsive and attractive fields successfully maneuvered the USV around obstacles and boundaries to reach the objective.

B. PROPOSAL FOR FUTURE STUDIES

Future work includes adding more obstacles and varying the spacing between them to test for local minimum and target reachability. Dynamic potential fields unknown to the USV would test the performance and efficiency of the piecewise linear potential field model. On the Clearpath USV, tuning the low-level controller would improve the performance (stability and tracking) of the USV. A camera and a laser range finder could be incorporated to identify

obstacles and targets. Potential fields would then be placed around those objects allowing the USV to maneuver safely and efficiently to complete the assigned task.

APPENDIX. THRUST COMMAND DATA

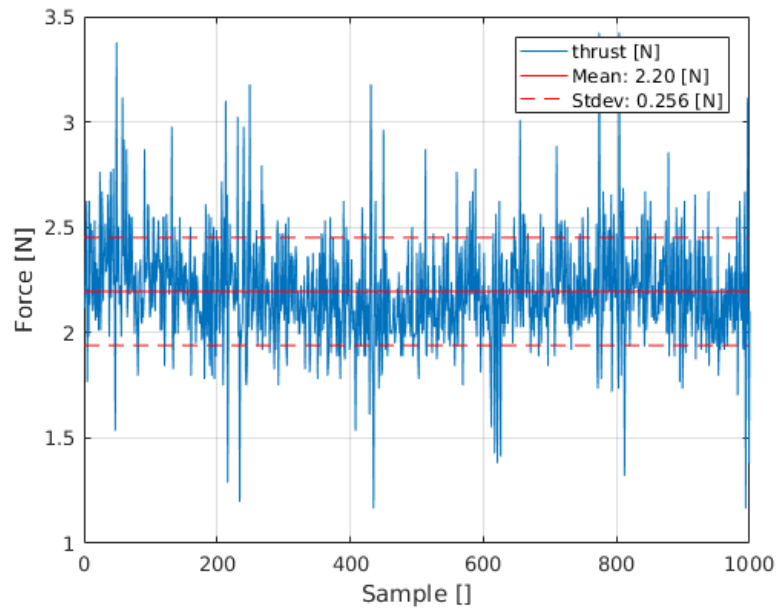


Figure 57. Forward Thrust Command 0.2

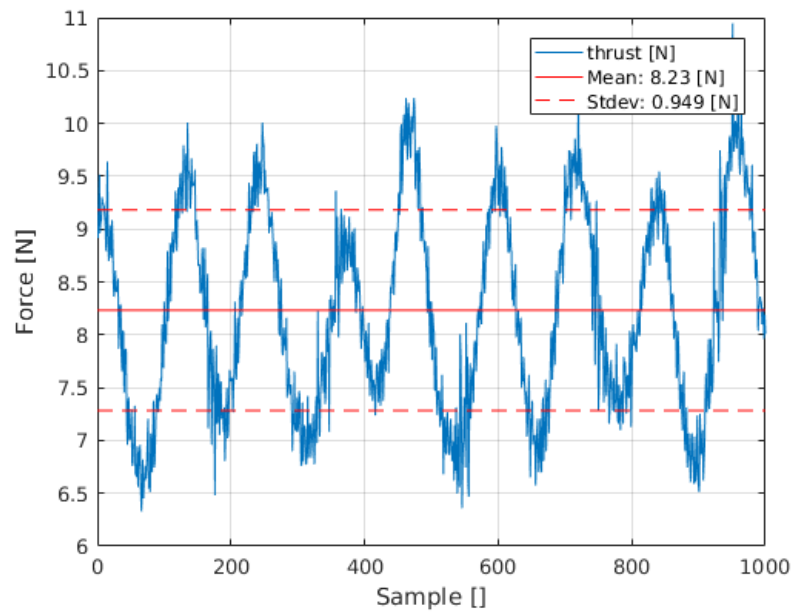


Figure 58. Forward Thrust Command 0.3

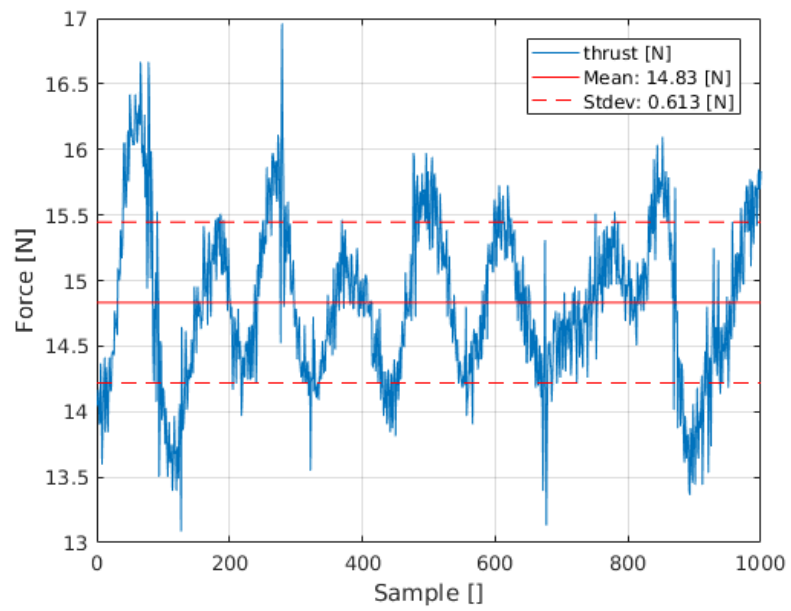


Figure 59. Forward Thrust Command 0.4

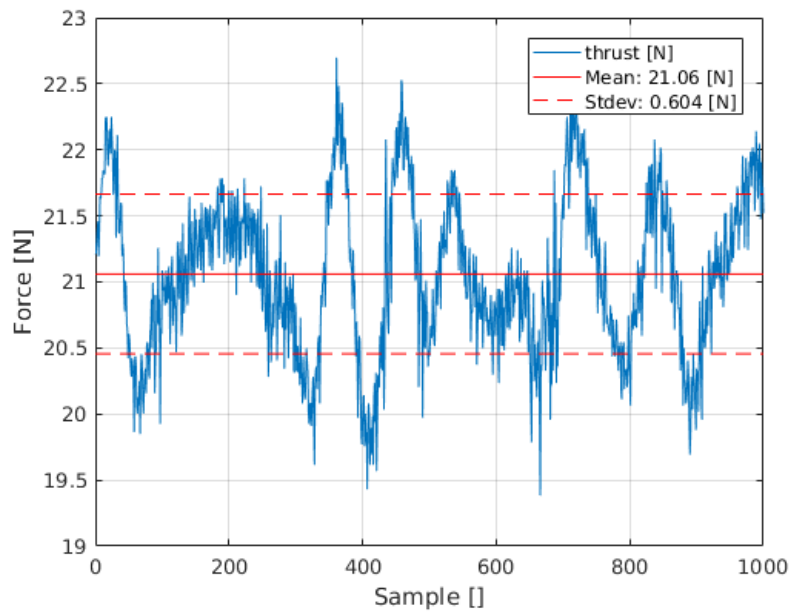


Figure 60. Forward Thrust Command 0.5

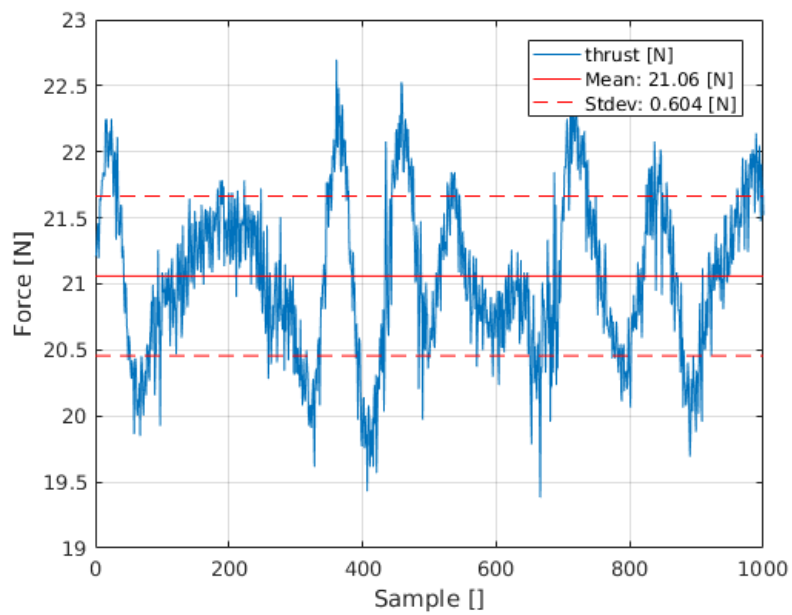


Figure 61. Forward Thrust Command 0.6

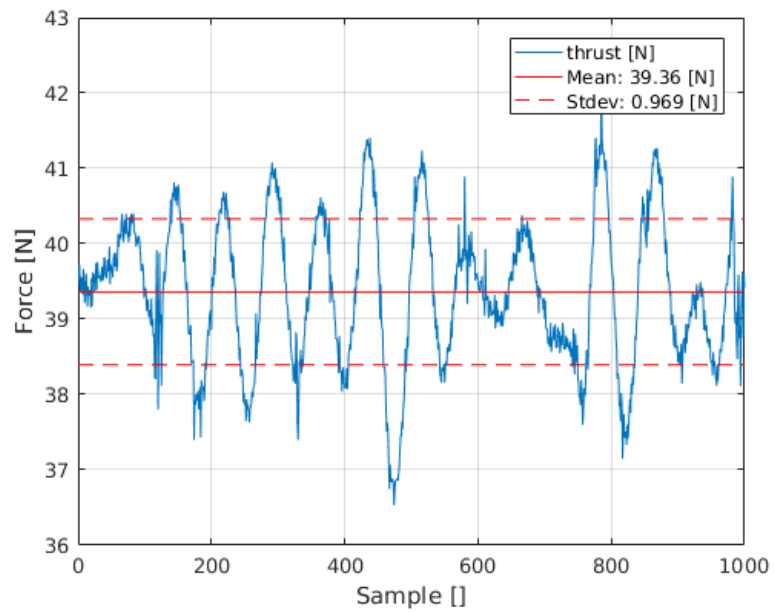


Figure 62. Forward Thrust Command 0.7

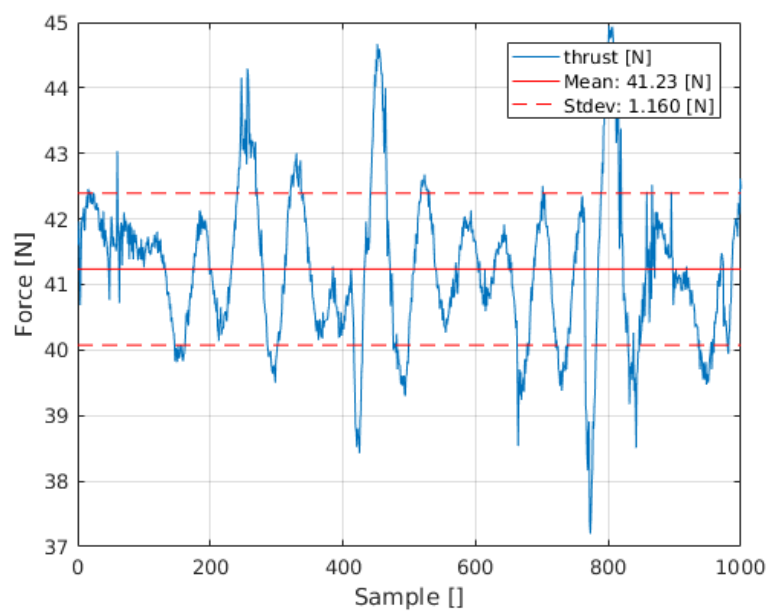


Figure 63. Forward Thrust Command 0.8

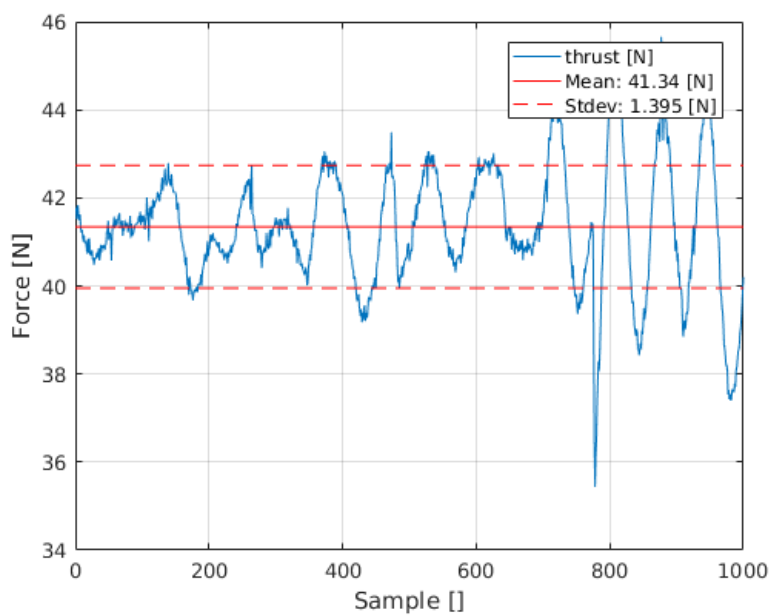


Figure 64. Forward Thrust Command 0.9

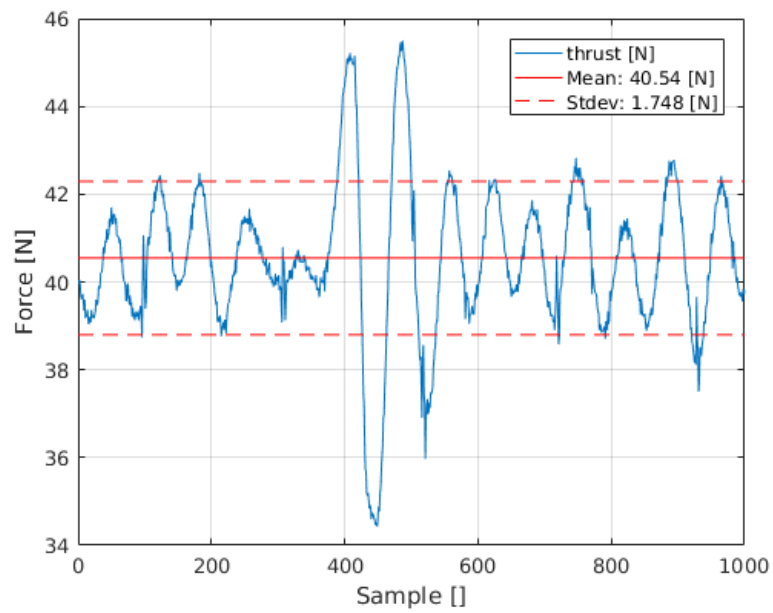


Figure 65. Forward Thrust Command 1.0

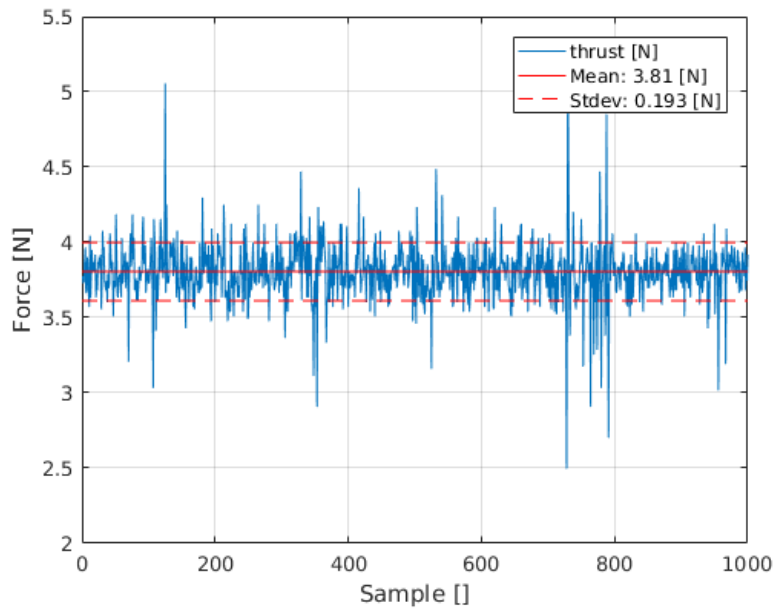


Figure 66. Aft Thrust Command 0.3

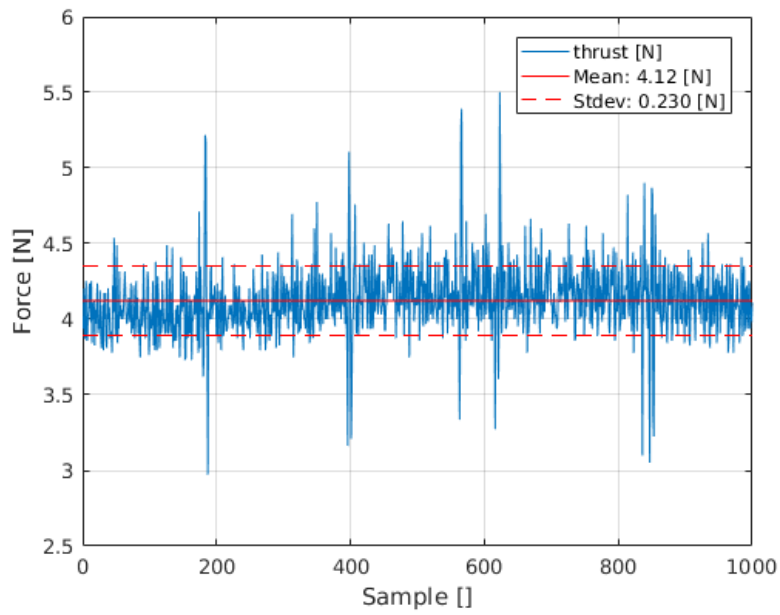


Figure 67. Aft Thrust Command 0.4

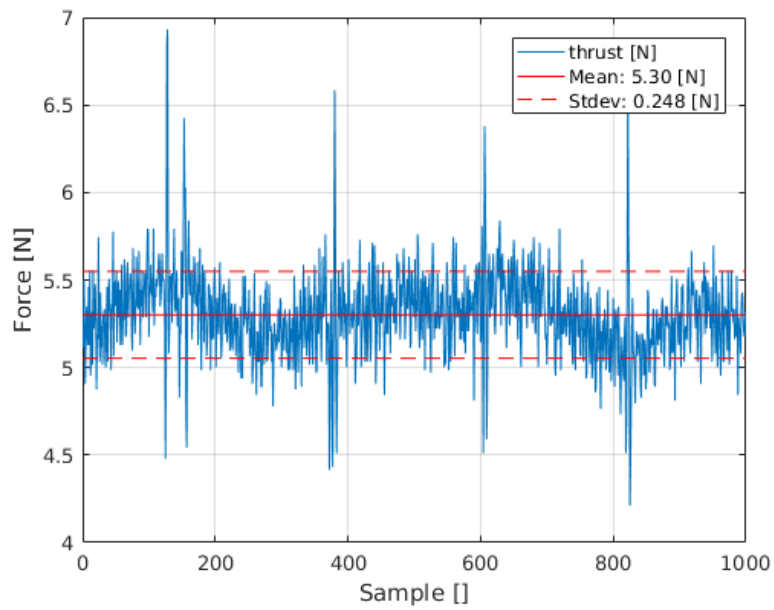


Figure 68. Aft Thrust Command 0.5

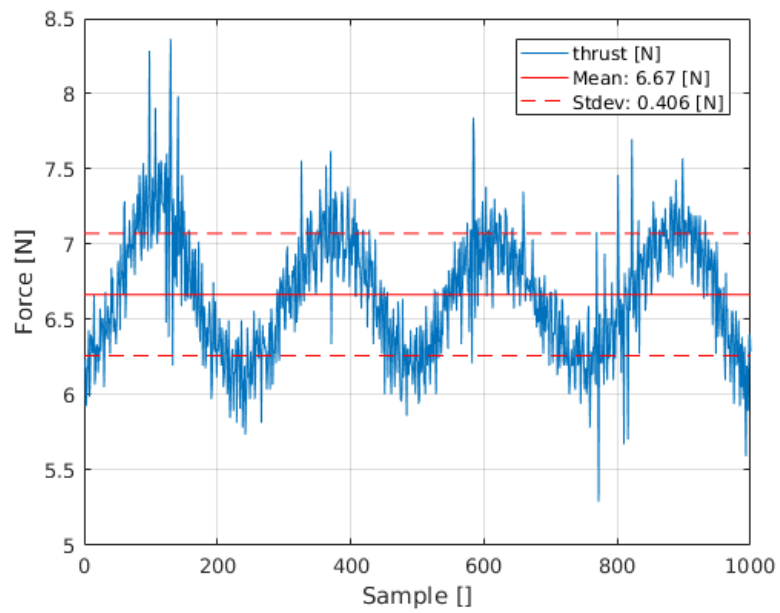


Figure 69. Aft Thrust Command 0.6

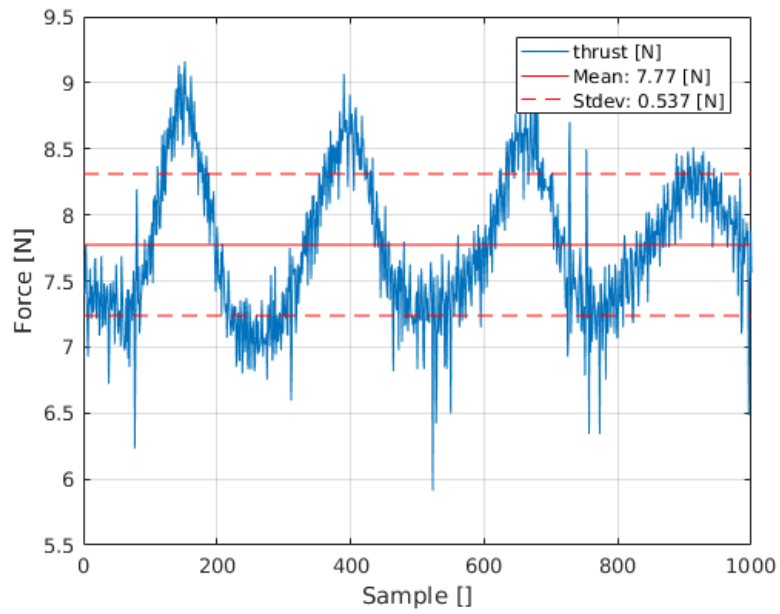


Figure 70. Aft Thrust Command 0.7

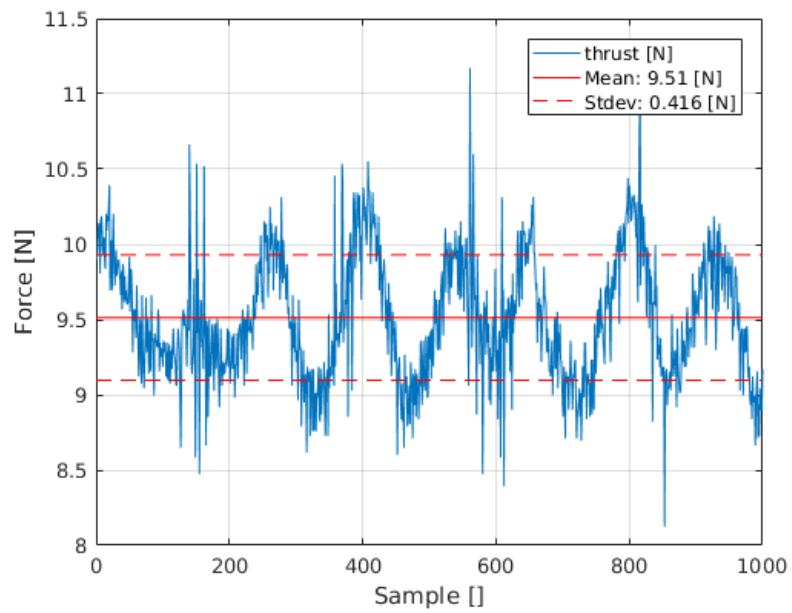


Figure 71. Aft Thrust Command 0.8

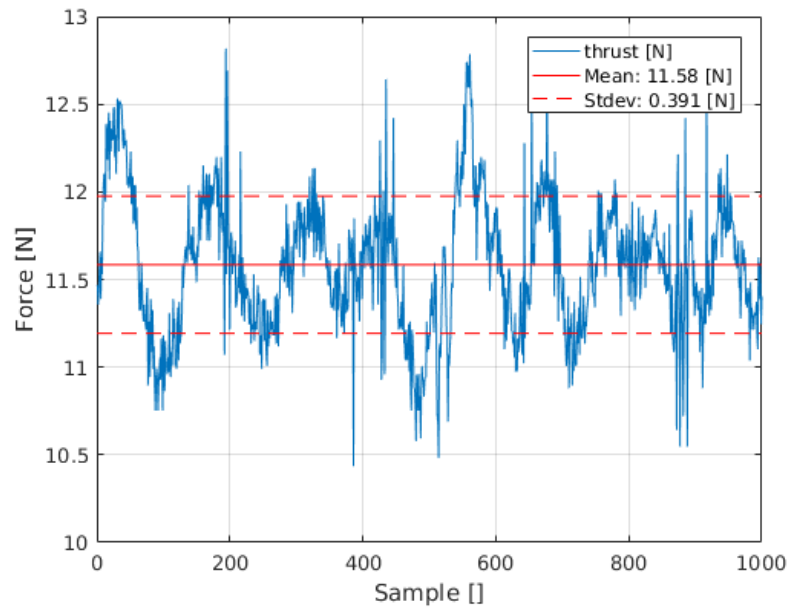


Figure 72. Aft Thrust Command 0.9

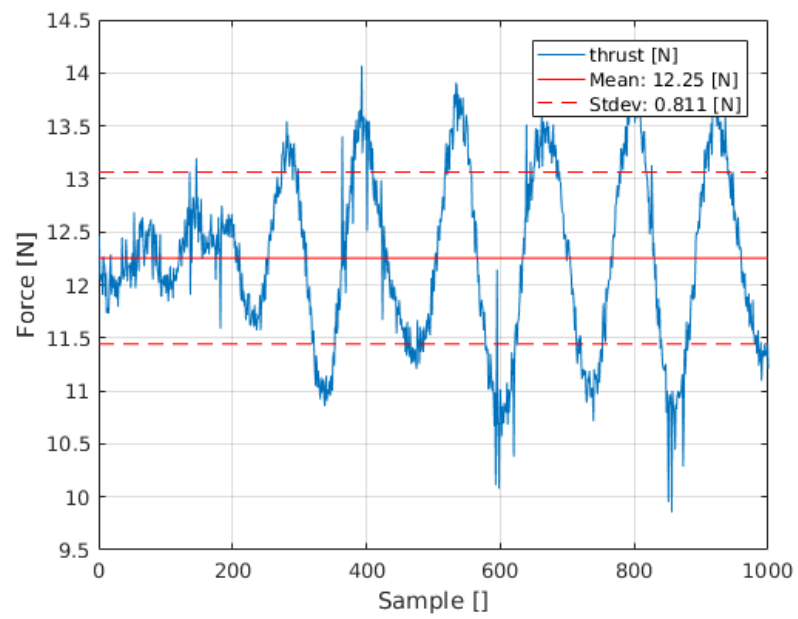


Figure 73. Aft Thrust Command 1.0

THIS PAGE INTENTIONALLY LEFT BLANK

LIST OF REFERENCES

- [1] Department of the Navy, "*The Navy unmanned surface vehicle (USV) master plan*, Program Executive Office Littoral and Mine Warfare (PEO LMW), Department of the Navy, Washington, DC, 2007.
- [2] Clearpath Robotics. (n.d.). Heron unmanned surface vessel. [Online]. Available: <https://www.clearpathrobotics.com/heron-bathymetry-unmanned-surface-vessel/>. Accessed Sept. 11, 2017.
- [3] D. Smalley. (2014, Oct.). The future is now: Navy's autonomous swarmboats can overwhelm adversaries. Office of Naval Research (ONR). Arlington, VA. [Online]. Available: <https://www.onr.navy.mil/Media-Center/Press-Releases/2014/autonomous-swarm-boat-unmanned-caracas.aspx>.
- [4] J. Latombe, *Robot Motion Planning*. Norwell, MA: Kluwer Academic, 1991, pp. 295–310.
- [5] Shaorong Xie *et al*, "The obstacle avoidance planning of USV based on improved artificial potential field," in *IEEE International Conference on Information and Automation (ICIA)*, Hailar, China, 2014, pp. 746–751.
- [6] Michael A. Goodrich, "Potential fields tutorial," Dept. of Computer Science, Brigham Young University, Provo, UT, unpublished.
- [7] T. I. Fossen, *Handbook of Marine Craft Hydrodynamics and Motion Control*. Chichester, West Sussex, England: Wiley, 2011.
- [8] T. I. Fossen, *Guidance and Control of Ocean Vehicles*. Chichester, West Sussex, England: Wiley, 1994.
- [9] M. Caccia, G. Bruzzone and R. Bono, "A practical approach to modeling and identification of small autonomous surface craft," in *IEEE Journal of Oceanic Engineering*, vol. 33, no. 2, pp. 133-145, Apr. 2008.
- [10] Google Maps. (2017). Lake El Estero, Monterey, CA [Satellite map]. Retrieved from <https://www.google.com/maps/@36.5963187,-121.8883422,356m/data=!3m1!1e3>

THIS PAGE INTENTIONALLY LEFT BLANK

INITIAL DISTRIBUTION LIST

1. Defense Technical Information Center
Ft. Belvoir, Virginia
2. Dudley Knox Library
Naval Postgraduate School
Monterey, California